

# 1 Cartesian Lattice Q-space Reconstructions

## 1.1 Overview

Between one-third to two-thirds of imaging voxels in the human brain's white matter are thought to contain multiple fibre bundle crossings[10], in which case the Diffusion Tensor model proposed by Basser et al.[9] breaks down. High Angular Resolution Diffusion Imaging (HARDI) [43] such as Diffusion Spectrum Imaging (DSI) [12], [47] or Higher Order Tensors [34], [8] and many more reconstruction methods have been proposed to overcome the limitations of the Diffusion Tensor. These methods can be divided into those who need specific acquisition parameterization for example they have to be sampled in one or more spherical grids like in Qball Imaging[45], or in a Cartesian grid like in Generalized Q-sampling Imaging (GQI) [50] and those which can be used independently of q-space structure like DTI. A further division considers the level of model assumptions for the diffusion process. Although all methods have some underlying assumptions we generally separate them in model-based and model-free. Model-based methods like the Single Tensor or Multi Tensor necessitate the fitting from a few to many parameters. On the opposite side with model-free methods fitting is not necessary and the directionality of the underlying tissue can be approximated by some re-parametrization or re-transformation of the signal. The latter is usually more efficient than fitting models with many parameters.

This document presents and evaluates different model-free methods for the reconstruction of orientation distribution functions using diffusion MRI data sampled on a Cartesian lattice in  $\mathbf{q}$ -space. This non-parametric nature of the algorithms described here allows for the identification of multiple fibre crossings. In addition a new method is presented named Diffusion Nabla Imaging (DNI) and a family of methods is defined called the Equatorial Inversion Transform (EIT). The EIT is a new way to represent and reconstruct the diffusion signal. Our results show that it can perform better or as good as the current state-of-the art methods i.e. DSI and GQI.

## 1.2 Theory

We start from the classical formulation shown in eq.1 of joint  $\mathbf{k}$ -space and  $\mathbf{q}$ -space imaging (Callaghan 8.3.1 p. 438)[11], [12] using the narrow pulse gradient spin echo (PGSE) sequence of Tanner and Stejskal.

$$RF(\mathbf{k}, \mathbf{q}) = \int \rho(\mathbf{v}) \exp(i2\pi\mathbf{k} \cdot \mathbf{v}) \int P_\Delta(\mathbf{v}, \mathbf{r}) \exp(i2\pi\mathbf{q} \cdot \mathbf{r}) d\mathbf{r} d\mathbf{v} \quad (1)$$

Here  $RF$  is the complex RF signal measured at spatial wave number  $\mathbf{k}$  and magnetic gradient wave number  $\mathbf{q}$ ,  $\rho$  is the local spin density (number of protons per unit volume contributing to the RF signal),  $\Delta$  is the diffusion time scale of the sequence,  $P_\Delta$  is the average diffusion propagator (transition probability distribution),  $\mathbf{v}$  is the voxel coordinate and  $\mathbf{r}$  is the diffusion displacement.

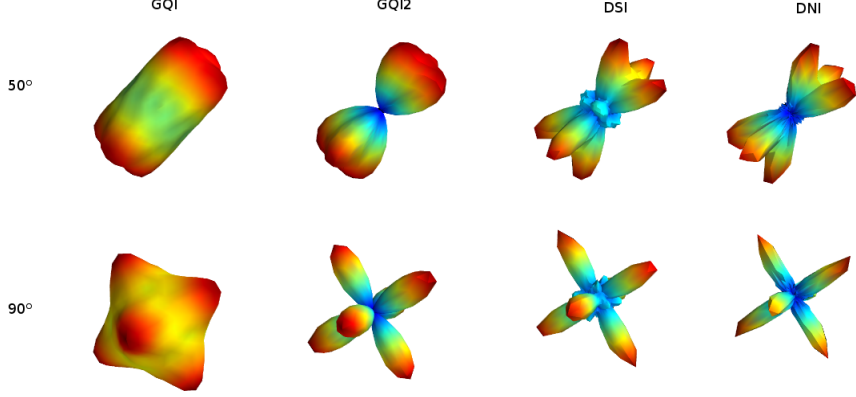


Figure 1.1: Showing the ODFs from two randomly oriented simulated 3-fibre crossings at  $50^\circ$ (top) and  $90^\circ$  angles between each other using different grid based reconstruction methods. The parameters used here are DSI: radial sampling  $2.1 - 6$ , hanning filter width  $36$  , GQI:  $\lambda=1.2$ , GQI2:  $\lambda = 3$ , DNI: standard.

The  $\mathbf{k}$ -space reconstruction gives us diffusion weighted image data  $S$  which reveal the average propagator  $P_\Delta$  of each voxel

$$S(\mathbf{v}, \mathbf{q}) = \int \rho(\mathbf{v}) P_\Delta(\mathbf{v}, \mathbf{r}) \exp(i2\pi\mathbf{q} \cdot \mathbf{r}) d\mathbf{r} \quad (2)$$

For the rest of the chapter we can drop  $\mathbf{v}$  as we assume that the formulation is the same for every voxel and  $\Delta$  because the time scale is the same for the entire sequence. We can also replace the spin density  $\rho(\mathbf{v})$  with  $S_0$  i.e. the measured signal without diffusion weighting  $\mathbf{q} = \mathbf{0}$ . Therefore we can write

$$S(\mathbf{q}) = S_0 \int P(\mathbf{r}) \exp(i2\pi\mathbf{q} \cdot \mathbf{r}) d\mathbf{r} \quad (3)$$

By applying the 3D Fourier transform in eq. 3 we can reconstruct the average propagator also known as the diffusion spectrum [46]

$$P(\mathbf{r}) = S_0^{-1} \int S(\mathbf{q}) \exp(-i2\pi\mathbf{q} \cdot \mathbf{r}) d\mathbf{r} \quad (4)$$

or diffusion propagator. It was shown by Wedeen et al. [46] that the dMRI signal is positive for any type of spin motion without net flux (i.e. spin displacements due to thermal molecular agitation) or other random fluxes such as intravoxel incoherent motion. Under this assumption we can replace in eq. 4 the complex signal  $S$  with its modulus  $|S|$

$$P(\mathbf{r}) = S_0^{-1} \int |S(\mathbf{q})| \exp(-i2\pi\mathbf{q} \cdot \mathbf{r}) d\mathbf{r} \quad (5)$$

The modulus of the signal coincides with the output of the standard MRI scanners as DWI and that simplifies the acquisition procedure. It represents the density of the average relative spin displacement in a voxel. In other words,  $P(\mathbf{r})d\mathbf{r}$  is a measure of the probability for a spin in a considered voxel to make, during the experimental mixing time  $\Delta$ , a vector displacement  $\mathbf{r}$ . We can visualize the propagator for every voxel as a 3D density volume (SEE Figure Introduction).

At each location, diffusion-weighted images are acquired for  $N = 515$  or less values of  $\mathbf{q}$ -encoding, comprising in  $\mathbf{q}$ -space the points of a cubic lattice within the sphere of five lattice units in radius. Therefore,

$$\mathbf{q} = \alpha \mathbf{q}_x + \beta \mathbf{q}_y + \gamma \mathbf{q}_z \quad (6)$$

with  $\alpha, \beta, \gamma \in \mathbb{Z}^+$  and  $(\alpha^2 + \beta^2 + \gamma^2)^{1/2} \leq 5$ . The signal is premultiplied by a Hanning window before Fourier transform in order to ensure a smooth attenuation of the signal at high  $q$  values.

Often to obtain data for the complete grid of 515  $\mathbf{q}$ -vectors (which also means that we need to collect 515 diffusion weighted volumes) is very time consuming and fewer number of unique  $\mathbf{q}$ -vectors are employed only at a single hemisphere usually between 102 to 257 points [25]. This is valid because the signal is symmetric therefore the vectors can be mapped on the other hemisphere to create the full  $\mathbf{q}$ -space.

Since we are mainly interested in the angular structure of the underlying tissue, we further simplify the data by taking the weighted radial summation of  $P(\mathbf{r})$

$$\psi_{DSI}(\hat{\mathbf{u}}) = \int_0^\infty P(r\hat{\mathbf{u}})r^2 dr \quad (7)$$

This defines the orientation density function (ODF) for DSI which measures the quantity of diffusion in the direction of the unit vector  $\hat{\mathbf{u}}$  where  $\mathbf{r} = r\hat{\mathbf{u}}$ .

Notice at this point that in order to find the ODF we have to create first the diffusion propagator by applying the Fourier transform on the lattice. Yeh et al.[50] proposed a direct analytical way to calculate a slightly different ODF using the Cosine transform.

In order to represent the average propagator in the scale of spin quantity Yeh et al.[50] introduced the *spin density function*  $Q$  which is estimated by scaling the average propagator  $P_\Delta$  with the spin density  $\rho$ , i.e.  $Q(\mathbf{r}) = \rho P(\mathbf{r}) = S_0 P(\mathbf{r})$ . From eq. 3 we obtain

$$S(\mathbf{q}) = \int Q(\mathbf{r}) \exp(i2\pi\mathbf{q} \cdot \mathbf{r}) d\mathbf{r} \quad (8)$$

We can apply the Fourier transform again in eq.8 and obtain

$$Q(\mathbf{r}) = \int S(\mathbf{q}) \exp(-i2\pi\mathbf{q} \cdot \mathbf{r}) d\mathbf{q} \quad (9)$$

Because  $Q(\mathbf{r})$  is real and  $S(\mathbf{q})$  is symmetric (even), i.e.  $S(\mathbf{q}) = S(-\mathbf{q})$ , we can use directly the Fourier Cosine transform (see 1.11.1) to calculate

$$Q(\mathbf{r}) = \int S(\mathbf{q}) \cos(2\pi \mathbf{q} \cdot \mathbf{r}) d\mathbf{q} \quad (10)$$

and obtain the “spin” orientation distribution function (SDF)  $\psi_{GQI}$  from an unweighted truncated radial projection

$$\psi_{GQI}(\hat{\mathbf{u}}) = \int_0^\lambda Q(r\hat{\mathbf{u}}) dr \quad (11)$$

$$= \int_0^\lambda \int S(\mathbf{q}) \cos(2\pi r \mathbf{q} \cdot \hat{\mathbf{u}}) d\mathbf{q} dr \quad (12)$$

$$= \int S(\mathbf{q}) \text{sinc}(2\pi r \mathbf{q} \cdot \hat{\mathbf{u}}) d\mathbf{q} \quad (13)$$

where  $\lambda$  is a constant called the diffusion sampling length. This parameter acts like a smoothing factor. The higher  $\lambda$  the more detailed the SDF will be but also more noisy. This ODF was used as the basis of the analysis of the GQI method. It provides a simple direct analytical solution of the ODF which can be written in a simple matrix form

$$\psi_{GQI} = \mathbf{s} \cdot \text{sinc}((6D \cdot G \circ \mathbf{b} \circ \mathbf{1}) \cdot G) / \pi$$

where  $\cdot$  denotes standard matrix or vector dot product,  $\circ$  denotes the Hadamard product,  $\mathbf{y}$  is  $\psi_{GQI}$  as a  $M$ -dimensional vector for every direction  $\hat{\mathbf{u}}$ ,  $\mathbf{s}$  is a vector with all the signal values,  $6D = 0.01506$  where  $D$  is a constant known as the free water diffusion coefficient,  $G$  is the  $N \times 3$  matrix with the gradient vectors,  $\mathbf{b}$  is the  $N \times 1$  matrix with the b-values and  $\mathbf{1}$  is the  $N \times 3$  incidence matrix where all values are equal to 1.

For a similar ODF like the one produced using DSI we need to take the weighted truncated radial projection. This will give us a different “spin” ODF which we symbolize with  $\psi_{GQI_2}$

$$\psi_{GQI_2}(\hat{\mathbf{u}}) = \int_0^\lambda Q(r\hat{\mathbf{u}}) r^2 dr \quad (14)$$

$$= \lambda^3 \int S(\mathbf{q}) H(2\pi r \mathbf{q} \cdot \hat{\mathbf{u}}) d\mathbf{q} \quad (15)$$

$$\text{where } H(x) = \begin{cases} \frac{2\cos(x)}{x^2} + \frac{(x^2-2)\sin(x)}{x^3}, & x \neq 0 \\ 1/3, & x = 0 \end{cases}$$

This equation can be similarly implemented with a simple matrix transform

$$\psi_{GQI2} = \mathbf{s} \cdot \mathbf{H}((6D \cdot G \circ \mathbf{b} \circ \mathbf{1}) \cdot G) \lambda^3 / \pi$$

and until today it hasn't been published with real or simulated data sets.

The addition of the spin density plays a very important role on normalizing the ODF and providing scalar or vector metrics for the analysis of dMRI data sets. GQI similarly with DSI expects the q-vectors to sit on a cubic lattice within a sphere. However, because of the direct analytical formulation of the GQI ODFs; the creation of the volumetric grid with the signal values is not necessary. This makes this GQI advantageous on memory and CPU efficiency. Furthermore, no Hanning filter is necessary.

A new method for the calculation of the real ODF is proposed here. This is based on the theoretical work done by Aganj et al. [1],[14] using two important theorems from Fourier Analysis

1. The Fourier transform of  $P(\mathbf{r})r^2 = -\nabla^2 E(\mathbf{q})$  where  $\nabla^2$  is the Laplacian operator (for proof see 1.11.2).
2. For a symmetric function  $E : \mathbb{R}^3 \rightarrow \mathbb{R}$  and for the arbitrary unit vector  $\hat{\mathbf{u}}$  we have  $\int_0^\infty E(r\hat{\mathbf{u}})dr = \frac{1}{8\pi^2} \int \int_{\hat{\mathbf{u}}^\perp} E(q)qdq d\phi$  where  $\hat{\mathbf{u}}^\perp$  is the plane perpendicular to  $\hat{\mathbf{u}}$  (for proof see section 1.11.3).

From eq. 7 we see that the integration is over  $P(r\hat{\mathbf{u}})r^2$ , therefore we can write

$$\psi_{DNI}(\hat{\mathbf{u}}) = -\frac{1}{8\pi^2} \int_{\hat{\mathbf{u}}^\perp} \int_0^\infty \nabla^2 E(q)qdq d\phi \quad (16)$$

where  $\phi$  is the angular rotation component operating on the plane perpendicular to  $\hat{\mathbf{u}}$ ,  $\nabla^2$  is the Laplacian operator and  $E(q) = S(q)/S_0$  is the normalized diffusion signal. Eq. 16 has the advantage that no Fourier transform is necessary. However we need to have a way to calculate the Laplacian of the signal. This can be analytically derived for a spherical grid [1] and we propose here that it can be directly calculated in a cubic grid using the standard 3D discrete Laplacian filter which is given by the 3D kernel defined

by the following three planes  $\begin{pmatrix} 0 & 0 & 0 \\ 0 & 1 & 0 \\ 0 & 0 & 0 \end{pmatrix}, \begin{pmatrix} 0 & 1 & 0 \\ 1 & -6 & 1 \\ 0 & 1 & 0 \end{pmatrix}, \begin{pmatrix} 0 & 0 & 0 \\ 0 & 1 & 0 \\ 0 & 0 & 0 \end{pmatrix}$ .

This is a function commonly used for image processing. From now on when we use the Laplacian operator in order to measure the directionality of the diffusion signal we will call this reconstruction method Diffusion Nabla Imaging as nabla ( $\nabla^2$ ) is the symbol for the Laplacian operator.

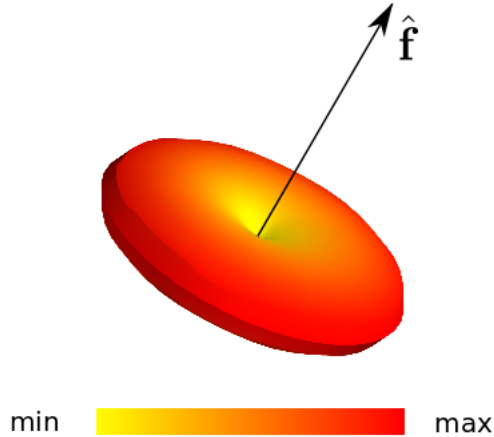


Figure 1.2: The diffusion signal has the beautiful property to be minimum along the direction of a fibre with unit direction  $\hat{f}$  and maximum along the equator defined by the plane perpendicular to that fibre direction. This property is the basic inspiration behind the EIT. In this picture the 3D surface plot of a simulated signal for a spherical grid acquisition with  $b$ -value 2000 is shown using a yellow-red colourmap.

### 1.3 Equatorial Inversion Transform

I propose an important theoretical construction called the Equatorial Inversion Transform (EIT) which creates a general formulation for the interpretation of the directionality of the diffusion signal. This idea is founded on two general properties of the diffusion signal: a) If we visualize the diffusion signal for a single fiber for all gradient directions we see that a shape is generated which is smallest towards the direction of the fiber and biggest on the plane perpendicular to that direction (see fig. 1.2). b) The diffusion signal is additive i.e.  $S(\hat{f}_1) + S(\hat{f}_2) = S(\hat{f}_1 + \hat{f}_2)$ , where  $\hat{f}_1, \hat{f}_2$  are the unit directions of the fibres. In simple terms the signal of 2-fibre crossing can be decomposed linearly to the signals of the two fibres that create the crossing. The same holds for any number of fibres in a crossing.

These are two very important geometric properties of the signal that we can try to exploit at the maximum by calculating equatorial integrals in order to identify the directionality of the signal.

Apart from the visual confirmation further supporting evidence that equatorial integration is crucial for derivation of directionality can be seen in eq. 16 where an equatorial integral which creates a connection between the real ODF and the signal. The Funk-Radon Transform (FRT) used by [45] is another example where equatorial integration is employed using the reconstruction sphere. We will see next that DNI and FRT are just a subset of the EIT.

$F$	$O$	Name	Comment
$II$	1	DNI≡EITL	calculates the real ODF without the complications of the FFT
$III$	1	EITL2	high resolution at low angles
$I$	1	EITS	impressive resolution without any preprocessing of the signal
$I$	0	'QBI'-like	similar to the Funk Radon Transform

Table 1.1: The Equatorial inversion transform (EIT) can be used to explain many other reconstructions algorithms.

With EIT the most important goal is to try to identify the correct directionality of the signal in the most accurate way by generating a spherical density. However it is possible to calculate as well the real ODF as defined by Wedeen et al. [46].

The EIT shown in eq. 17 consists of an integration along the equator and along radial lines. A function  $F$  of the signal is multiplied by a radial weighting function  $O$ . This construction is a generalization of the previous ODFs and it can support successfully many different function families for  $F$  and  $O$  which can all more or less accurately identify the directional distribution of the signal. More precisely the EIT is defined as

$$\psi_{EIT}(\hat{\mathbf{u}}) = \int_{\hat{\mathbf{u}}^\perp} \int_0^\infty F(E(q))O(q)dq d\phi \quad (17)$$

where  $F$  could be for example any of the following functions

$$F(E(q)) = \begin{cases} E(q) & (I) \\ -\nabla^2(E(q)) & (II) \\ \nabla^4(E(q)) & (III) \\ \dots \end{cases} \quad (18)$$

and  $O$  could be for example any of the following functions

$$O(q) = \begin{cases} 1 & (0) \\ q & (1) \\ q^2 & (2) \\ \dots \end{cases} \quad (19)$$

In table 1.1 we see that different functions of  $F$  or  $O$  can generate older well known or new distribution functions on the sphere. With  $F(E(q)) = -\nabla^2(E(q))$  and  $O(q) = q$  we can generate  $\psi_{DNI}$  which is theoretically identical to the DSI real ODF( $\psi_{DSI}$ ). If  $F(E(q)) = E(q)$  and  $O(q) = 1$  then this is

similar with the Funk Radon Transform (used in Qball imaging) but applied to multiple spherical shells. However, we can also try to use different functions like  $F(E(q)) = -\nabla^4(E(q))$  and  $O(q) = q$  which can potentially increase the amount of directional information beyond than the standard ODFs. Before starting investigating the realms of EIT we should first give a short overview of other methods commonly found in the literature. These are grid-based, mostly non-grid based and usually parametric.

## 1.4 Other methods

Pickalov et al.[37] proposed a new method for reconstructing the diffusion propagator by applying an iterative inverse Radon transform on measurements along many radial lines; computing 1D tomographic projections to reconstruct the 3D EAP. This technique measures DW images along a few radial lines of q-space but still requires hundreds of samples to reliably recover the EAP. Currently, to reconstruct the EAP, the state-of-the-art model-free techniques apart from diffusion spectrum imaging are hybrid diffusion imaging (HYDI) [49] and multiple q-shell diffusion propagator imaging (mq-DPI)[20]. HYDI acquires the signal values on 5 concentric spherical q-space shells, then interpolates to a cubic grid and applies the standard Fourier transform in the same way as DSI. In mq-DPI the EAP is calculated by solving Laplace's equation for the diffusion signal using a real and symmetric modified spherical harmonic basis. The EAP can be found analytically by the inversion of a linear system using Laplace-Beltrami regularization. In addition exact q-ball imaging (EQBI)[13] provides a different method to calculate the ODF analytically using multiple spherical q-space shells and similarly Aganj et al.[2], proposed an analytical solution for the multi-shell case by incorporating a mono-exponential or bi-exponential model (CSA-ODF). Another distribution on the sphere was proposed by Özarslan et al.[35] named diffusion orientation transform (DOT). This method calculates a different statistic  $P(r_0\hat{\mathbf{u}})$ , the probability of finding the particle initially at the origin, at the point  $r_0\hat{\mathbf{u}}$  using spherical harmonics. Not surprisingly there is a relationship connecting CSA with DOT which is

$$\psi_{CSA}(\hat{\mathbf{u}}) = \int_0^\infty DOT(r\hat{\mathbf{u}})r^2 dr \quad (20)$$

Jansons et al. [23] proposed a different function on the sphere than the ODFs described above, to be used on data sets acquired on a single spherical q-space shell. They called this spherical function persistent angular structure (PAS). This method has very good angular resolution because it uses the principle of maximum entropy however it is rather slow as it uses nonlinear fitting in order to identify many parameters. PAS is a statistic on the sphere defined as  $PAS(\hat{\mathbf{u}}) = \exp(\lambda_0 + \sum_{j=1}^N \lambda_j \cos(\mathbf{q}_j \cdot k\hat{\mathbf{u}}))$  where  $\lambda$  are the unknown parameters,  $k$  is constant and  $N$  is the number of DWIs. The relationship  $\int PAS(\hat{\mathbf{u}}) \exp(i\mathbf{q}_j \cdot k\hat{\mathbf{u}}) d\hat{\mathbf{u}} = E(\mathbf{q}_j)$  provides the bridge between PAS and the diffusion signal ( $E(\mathbf{q})$ ).

The first reference of using spherical harmonic expansions with diffusivity profiles, which are now very favorable in the literature, was by Alexander et al.[3]. Qball imaging was introduced by Tuch [45] and a new ODF defined as  $\psi(\hat{u}) = \frac{1}{Z} \int_0^\infty P(r\hat{u})dr$  where  $Z$  is a normalization constant. It was later provided for QBall imaging a fast and analytical solution using spherical harmonics (SH) and Laplace-Beltrami regularization [18]. Tournier et al. [41],[42] introduced a spherical deconvolution method where first the SH coefficients were reconstructed by , then single fiber ODFs are used as a deconvolution kernel estimated from the real data. Then the sharper fODF was obtained by a simple linear transformation [19]. Other deconvolution approaches were proposed in [40] and [51].

On Tensor related methods we have the classical SingleTensor [9], Sticks&Ball[10], Multi-Tensor[36][27] and Higher Rank Tensors [34],[8]. In addition there are also model based methods which try to calculate non-Gaussian properties for example the Kurtosis Tensor [24],[28] which is used in Diffusion Kurtosis Imaging (DKI).

Finally, new model-based methods are emerging which are trying to calculate statistics like the axonal thickness distribution from dMRI data sets. These are usually based on modeling free and restricted components; CHARMED [5][7], AxCaliber [6] and the orientation invariant ActiveAx[4] are some well known methods of this type. Q-space Imaging(QSI) can be used to identify distributions of axon-diameter too[33].

## 1.5 Implementation

### 1.5.1 Standard EIT

Eq. 16 and 17 can be implemented in a standard way by evaluating the 3D signal on the grid multiple times for every direction  $\hat{u}$  as shown in fig. 1.3(A). This suggests that if for example we use a reconstruction sphere of 642 vertices and the radial integration ( $q$ ) takes place in 30 steps and the equatorial ( $\phi$ ) in 63 steps then we need to interpolate  $642 \times 30 \times 30 \simeq 1.2$  million times on the cubic grid. For this reason I invented Fast EIT a new method that needs an order of magnitude less evaluations.

In this document whenever we use the prefix s in front of a method that will mean that this was calculated with the standard EIT algorithm. For example if standard EIT is used for DNI we will write sDNI or sEITL. Of course sDNI and sEITL are equivalent.

### 1.5.2 Fast EIT

A much faster algorithm than the standard EIT is described here. The main idea is that we can store the sum of the radial integrals for every vertex in the reconstruction sphere and then we can also precompute the indices of the vertices that are near the equator of every vertex (inside an equatorial zone) see fig. 1.3(B). After these calculations the spherical distribution function can be

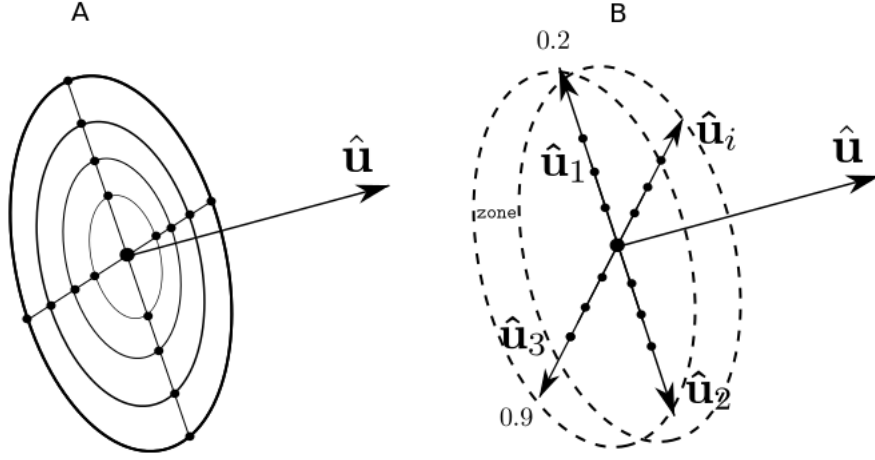


Figure 1.3: (A)Standard EIT vs (B)Fast EIT algorithm. Fast EIT is an order of magnitude faster than standard EIT. The key idea here is that reduce computations by storing the sum of the radial integrals for every vertex in the reconstruction sphere and then we can also precompute the indices of the vertices that are near the equator of every vertex (inside an equatorial zone).

approximated with much less operations. The full algorithm is given in 1. The input is the vertices  $\hat{u}_i$  of the reconstruction sphere and the normalized signal  $E$ . Then for every point of the reconstruction sphere  $\hat{u}_i$  we save the indices of the vertices  $j$  of  $\hat{u}_i$ , which are inside an equatorial zone, in list  $J_i$ . The width of the equatorial zone  $z$  is a constant set empirically to  $5^\circ$ . If a very highly dense reconstruction sphere is used with more than 642 vertices which is the one we used then the zone can be smaller. That can potentially increase the angular resolution of the method.

At the next stage we calculate sums along every radius on the direction of  $\hat{u}_i$  in the following way  $\mathbb{B}(\hat{u}_i) = \sum_{k=0}^n F(E(q_k \hat{u}_i)) O(q_k \hat{u}_i)$  and obtain the final EIT ODF as the average of the sums in the equator  $\psi_{EIT}(\hat{u}_i) = \frac{1}{N_i} \sum_{j \in J_i} \mathbb{B}(\hat{u}_j)$  where  $F$  is evaluated with trilinear for example interpolation on the lattice and  $N_i$  is the number of indices in  $J_i$ .

In section 1.8.1 the standard EITL (sEITL) is compared with fast EITL. In fig. 1.8.1 we can see that the fast EIT has very similar results with the standard EIT therefore from now on whenever we see EIT written in this document we will assume that the fast version is used.

## 1.6 Peak Finding

After we have generated the ODFs we need to find the peaks (local maxima) from which we can easily approximate the direction of the fibres. Peak finding

---

**Algorithm 1** Fast Equatorial Inversion Transform

---

**Input**  $U = \{\hat{u}_1 \dots \hat{u}_m\}$ , E**Output**  $\psi_{EIT}$ **For each**  $\hat{u}_i$  **Do**

$$J_i = \{j : |\arccos(\hat{u}_i \cdot \hat{u}_j)| \leq z\}$$

**For each**  $\hat{u}_i$  **Do**

$$\mathbb{B}(\hat{u}_i) = \sum_{k=0}^n F(E(q_k \hat{u}_i)) O(q_k \hat{u}_i)$$

where  $F(E(q_k \hat{u}_i))$  is interpolated on the lattice.

$$\psi_{EIT}(\hat{u}_i) = \frac{1}{N_i} \sum_{j \in J_i} \mathbb{B}(\hat{u}_j)$$

where  $N_i$  is the number of indices in  $J_i$ .

---

**Algorithm 2** Peak Finding with a Symmetric Ordered Sphere

---

**Input** ODF  $\psi$ , faces  $\Phi$ **Output** peaks  $P$  and indices  $I$ **For each** face  $\Phi_i$  **Do**

$$f_0, f_1, f_2 = \Phi_i$$

$$d_0, d_1, d_2 = \psi[f_0], \psi[f_1], \psi[f_2]$$

**If**  $d_0 \geq d_1$  **and**  $d_2$  **Do**

$$P[f_1] = P[f_2] = 0$$

**continue**

---

can be non-trivial if there are many local maxima in the ODFs or the ODFs are noisy. Here we present an algorithm (??) which reduces the amount of small local variations and returns a number of sorted peaks and their indices in the reconstruction sphere. The input of this algorithm is  $\psi$  (ODF) and the faces of a symmetric on the z-axis evenly distributed sphere (see fig. 1.6C).

We have constructed a sphere which is symmetric over the z-axis and the faces of the sphere are also ordered along the z-axis. The same sphere was used in [50] for GQI reconstructions. Every face contains the 3 indices which indicate at the 3 different points that create the triangle(face) of the sphere. The idea here is that we can travel from face to face and nullify all points on a face which are lower than the higher value of the face. At the end only local maxima will survive the procedure. The algorithm is presented in detail in alg. 2.

The sphere we use is of course discrete and therefore it adds some constraints on the angular resolution (worst case  $\pm 4.96^\circ$ ) of the peaks found from the ODF. In addition the proposed Peak Finding algorithm can reduce slightly more the angular resolution. For example in Fig.1.6A+B we show that if point **a** was a local maxima then only points **b** could be alternative local maxima for **a** but none of the unlabeled points could be a second peak. Nevertheless we found alg. 2 to be extremely useful and fast. The same algorithm was used also in [50] but it was not documented as such.

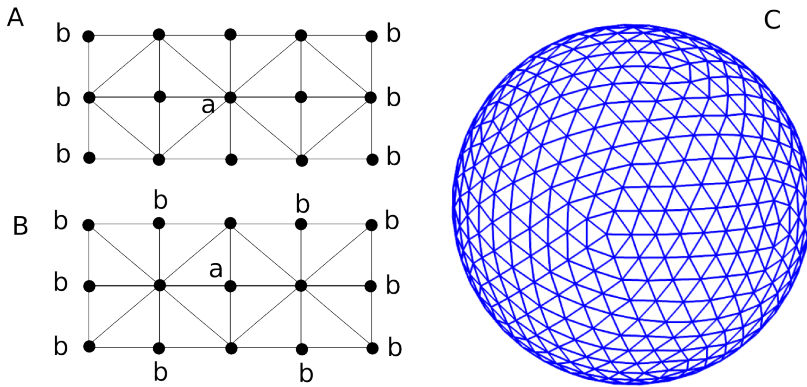


Figure 1.4: A,B: Imagine that point **a** is a local maximum for all its neighboring faces then only at **b** are other possible local maxima. This simple illustration shows that the triangulation of the sphere is important for the determination of closed peaks and that peaks which belong to the same triangle cannot be determined. C: the sphere used for ODF reconstructions consisting of 642 vertices and 1280 faces produced by subdivisions of the icosahedron.

## 1.7 Spherical Angular Smoothing

All current non-parametric dMRI reconstruction algorithms use some type of “smoothing” to reduce the effect of noise in the real data sets. DSI is using hanning filter and then avoiding sampling from low values in  $\mathbf{r}$ -space. In GQI, smoothing is controlled from a scalar parameter; the diffusion sampling length and in spherical harmonic inversion methods [21],[1] the amount of smoothing is controlled by using only a number of the first components of the SH series.

All these approaches smooth and calculate the ODFs simultaneously. We propose something different. That the ODF can be calculated initially and then smoothed using for example the following operator shown below in matrix form

$$W = \exp\left(\frac{\mathbf{U} \cdot \mathbf{U}^T}{s}\right)$$

where  $\mathbf{U}$  is the an  $N \times 3$  matrix holding the  $N$  points of the ODF reconstruction sphere and  $s$  is a smoothing parameter acting like the variance. At the next step we can smooth any  $\text{ODF}(\psi)$  creating a new  $\text{ODF}(\psi')$  in the following way

$$\psi' = \psi \cdot \frac{W}{\sum_j W_j} \quad (21)$$

where  $j$  denotes row indexing,  $\sum_j W_j$  acts as a normalization for the angular weighting  $W$ ,  $\psi$  is the initial ODF and  $\psi'$  is the smoothed ODF . The

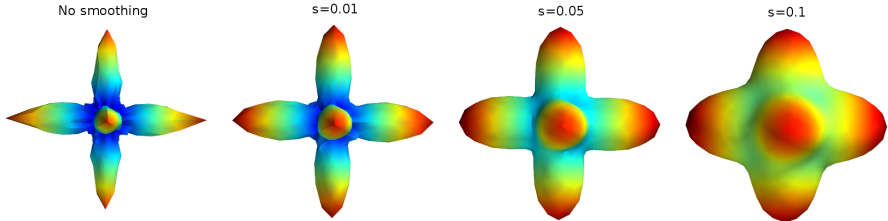


Figure 1.5: An example of spherical angular Gaussian smoothing applied with different smoothing factors on the distribution function of a triple-fibre crossing on the left. The simulation was used using (Sticks&Ball) model with diffusivity value 0.0015,  $S_0=100$ , and Gaussian noise with SNR 20.

advantage of this method is that it is more comprehensive and direct. Also it uses information from all directions simultaneously. Similar operators can be constructed that weight more lower or higher peaks. The operator shown here weighs more peaks that are closer in angular distance. In fig. 1.5 we see the effect of this equation on a simulated triple-fibre crossing; distorted with Gaussian noise with SNR 20 and reconstructed as a EITL density function which we have .

We can easily see in fig. 1.5 that when we increase the smoothing factor  $s$  small noisy peaks; as seen in the center of the unsmoothed spherical function can be easily removed. However, with too much smoothing even the longer peaks can lose their definition. This spherical operator can help to set the trade-off between noise and signal and it can also simplify the peak finding process i.e. finding the underlying primary fibre directions as this problem is much easier on smooth surfaces.

Finally, we believe that by decoupling the smoothing from the reconstruction phase we have an important advantage and that is that we can reduce more strongly and independently the effect of the noise to our data. Many spherical operators added as a plugins which is uncontrolled from the reconstruction phase and can work with any function on the sphere. For example Eq. 21 can be used with any function on the sphere.

## 1.8 Comparisons and Results

Validation of reconstruction and tractography algorithms is not straightforward due to the lack of relevant gold standards. Simulated voxels and digital phantoms is a useful way to overcome this difficulty and test new methods. After the simulation results we also show results with real human data sets.

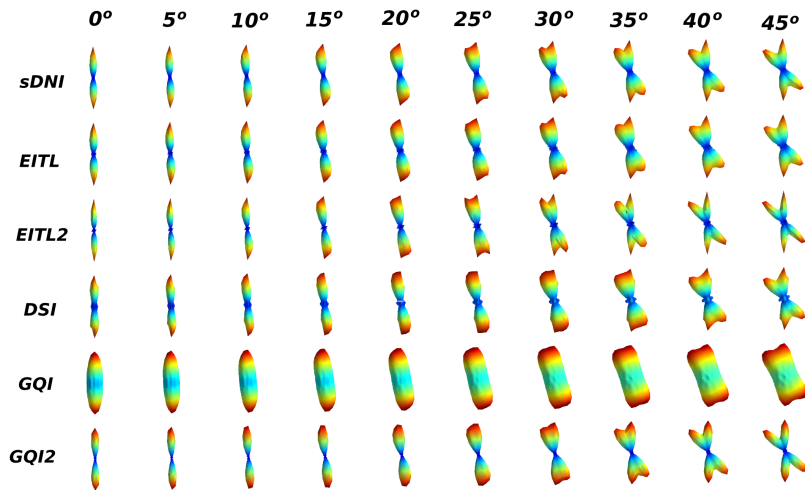


Figure 1.6: Visualizing ODFs created from different reconstruction methods sDNI (sEITL), EITL, EITL2, DSI, GQI, GQI2. These are based on simulations of 2-fibre crossings from  $0^\circ$  to  $90^\circ$  at steps of  $5^\circ$  using eq. 22. We can see that standard DNI (sDNI), EITL and EITL2 can resolve the correct angular fibre directions at lower angles than the other methods. For example see column at angle of  $25^\circ$ .

Known	Measured	AS
(1,0,0), (0,1,0)	(0,0,1)	0
(1,0,0), (0,1,0)	(0,1,0)	1
(1,0,0), (0,1,0)	(0, $\sqrt{2}/2$ , $\sqrt{2}/2$ )	$\sqrt{2}/2$
(1,0,0), (0,1,0), (0,0,1)	(1,0,0), (0,0,1)	2

Table 1.2: Examples of angular similarity (AS) behaviour with simple unit vector sets.

### 1.8.1 Multi-fibre Simulations

For single voxel simulations we used the model proposed in Behrens et al.[10]; the multi-compartment model also known as Sticks and Ball which simulates the diffusion signal as

$$S_i = S_0 \left( \left( 1 - \sum_{j=1}^N f_j \right) \exp(-b_i d) + \sum_{j=1}^N f_j \exp(-b_i d \cos(\theta_{ij})^2) \right) \quad (22)$$

where  $\theta_{ij}$  is the angle between gradient direction  $\hat{\mathbf{g}}_i$  and fibre(stick) unit direction  $\hat{\mathbf{u}}_j$ . The amount of representation for every fibre is given by  $f$  and  $d$  is the diffusivity value for the entire model. A Multi Tensor [27] approach was also created for digital phantoms using the formula

$$S_i = S_0 \sum_{j=1}^N \exp(-b \hat{\mathbf{g}}^T D_j \hat{\mathbf{g}}) \quad (23)$$

where  $D_j$  is the diffusion tensor for every fibre  $j$ .

A comparison method/metric is needed in order to evaluate the new/old reconstruction methods discussed in this document. The standard procedure is to calculate the similarity between the measured and simulated “golden truth” data sets. We want to calculate the angular precision of the ODFs from simulations derived from eq. 22. We define a new similarity metric called angular similarity (AS) which computes the cosine distance of the best match between the set of measured fibre orientations and the known set of simulated fibres. This metric will be used to compare 2-fibre and 3-fibre crossings. AS is 0 when there is no match i.e. angular distance is maximum ( $90^\circ$ ), 1 when 1 fibre is matched ( $0^\circ$ ), 2 when 2 fibres are matched and 3 when 3 fibres are matched. In table 1.2 we show a few examples of AS behaviour with simple unit vector sets.

If our “golden” (known) set consists of  $g = [(1,0,0), (0,1,0)]$  and the measured set consists of  $m = [(0,0,1)]$  then AS=0. If the measured set was  $m = [(0, \sqrt{2}/2, \sqrt{2}/2)]$  then AS is  $\sqrt{2}/2$ . This is because according to the AS definition we have  $AS(g,m)=\max(|g[0] \cdot m[0]|, |g[1] \cdot m[0]|)=\sqrt{2}/2$ . If  $g = [(1,0,0), (0,1,0)]$  and  $m = g$  then  $AS(g,m)=\max(|g[0] \cdot m[0]| + |g[1] \cdot m[1]|, |g[0] \cdot m[1]| + |g[1] \cdot m[0]|)=2$ .

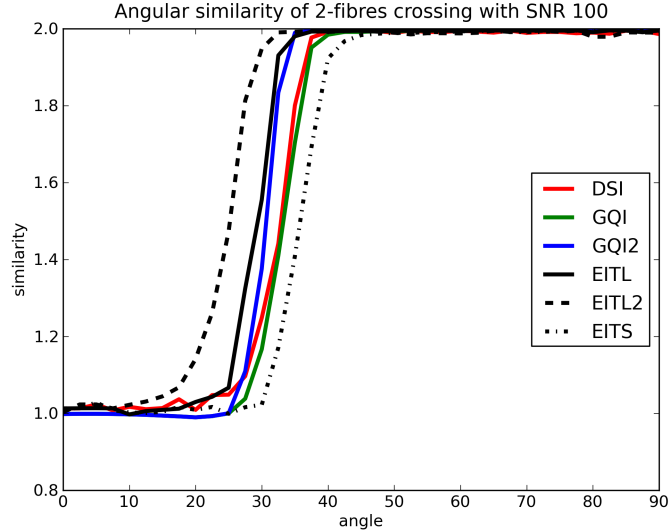


Figure 1.7: Average angular similarity of 2-fibre crossings with SNR 100

We created an experiment where we set two fibres at an increasing angle of  $2.5^\circ$  from  $0^\circ$  to  $90^\circ$  and then rotate them uniformly around 200 random axes. This operation produces 7400 simulated ODFs and the results are shown in fig. 1.7, 1.8 with different signal to noise ratio. For these simulations noise was normally distributed. What we see in the figures is the average angular similarity where the average is calculated from the 200 random orientations for the same angle.

We can easily observe in fig. 1.7 that EITL2 can resolve more accurately fibre crossings at low angles and continue performing decently well even at higher angles  $> 50^\circ$ . Then EITL is doing better than DSI, GQI, GQI2 and EITS at low angles and very well at high angles as well. GQI2 performs better than DSI, GQI, and ETS. It is also impressive that EITS can have such a good performance although it is such a simple operation. In summary we say from the that EITL2>EITL>GQI2>DSI>GQI>EITS where  $>$  means better average angular similarity. The same pattern takes place even when we increase the noise level see for example fig. 1.8. We will see next that the same pattern will take place even with 3-fibre crossings and high levels of noise.

We also measured the accuracy in 3-fibre crossings. Therefore, we created an experiment where the 3-fibres would always have the same angular distance between each other. That distance would increase from  $0^\circ$  to  $90^\circ$  with steps of  $2.3^\circ$  on average and all 3 fibres would be reoriented 200 times. That gave 8000 simulated crossings.

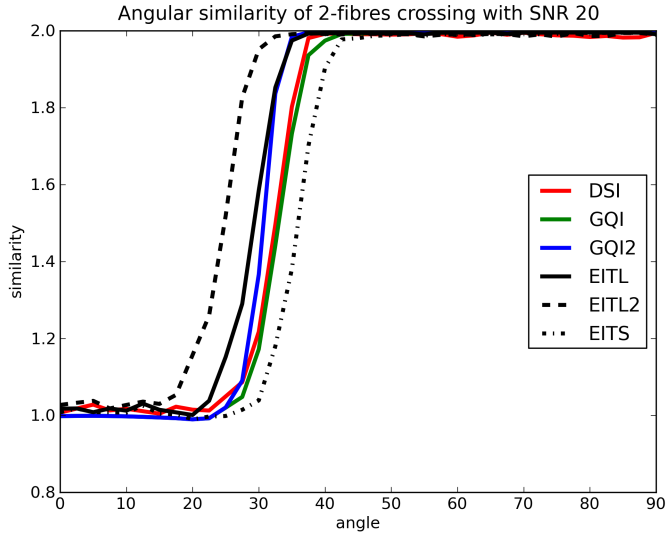


Figure 1.8: Average angular similarity of 2-fibre crossings with SNR 20.

The results of the 3-fibre crossings shown in fig. 1.9 and 1.10 were very similar with those of the 2-fibre crossings; EITL2 scores higher at low angles with a bit reduced performance at high angles and EITL doing better with low angles than the rest of the methods and also having high accuracy on larger angles.

These concentrative plots give strong evidence that both DNI (EITL) and in general EIT can be used to accurately generate spherical distribution functions for the determination of the directional information of the diffusion signal and that these can do better or similar to the current state-of-the-art grid-based reconstruction methods i.e DSI and GQI. Also the addition of noise didn't manage to affect the determination of the fibre directions considerably.

Furthermore, we can also see that GQI2 can do better than DSI, GQI and that EITS gives results that are very similar to GQI. The parameters used for these simulations were DSI: radial sampling 2.1 – 6, hanning filter width: 36 , GQI:  $\lambda=1.2$ , GQI2:  $\lambda = 3$ , and EITS, EITL, EITL2 were all calculated with the standard options zonal width ( $z = 5^\circ$ ), grid size  $17 \times 17 \times 17$ , radial sampling 0 – 5 with 0.1 steps and no further post-processing or smoothing was used. All methods were using the same reconstruction sphere with 642 vertices and 1280 faces.

Finally, we should stress that we have never seen any considerable differences between spherical functions created using the standard or fast EIT. For example a simple test for the 3-fibre case as seen in fig. 1.8.1 can show that there is close agreement between the two methods i.e. their results are nearly

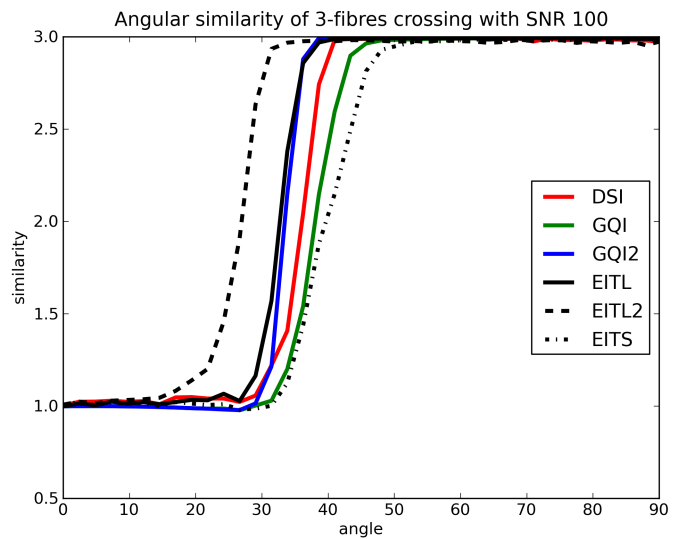


Figure 1.9: Average angular similarity of 3-fibre crossings with SNR 100.

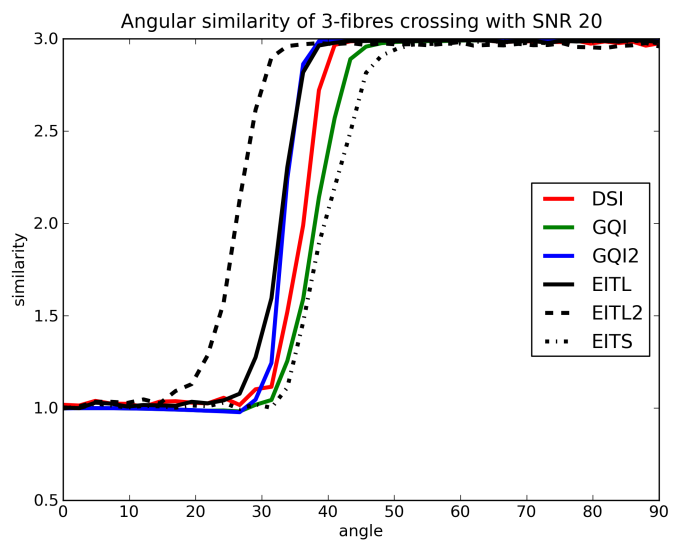


Figure 1.10: Average angular similarity of 3-fibre crossings with SNR 100.

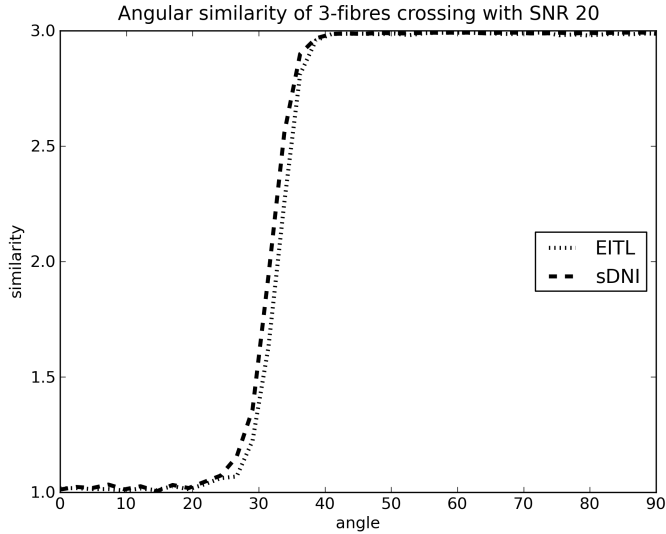


Figure 1.11: This diagram shows that when we compute EITL with the fast or standard method the results are nearly equivalent. We show here that the mean angular similarity for the case of 3-fibres crossings is very similar when using standard DNI or or fast DNI (EITL).

equivalent. Therefore we can conclude that the fast EIT is great approximation of the standard EIT.

### 1.8.2 Digital Phantoms

A digital phantom generation tool was developed which can simulate the diffusion weighted signal for one or more fibres represented by different discrete 3D orbital functions. This work is an extension of the phantom developed by Correia et al. [15] who supported only semi-circular functions with analytically calculated derivatives.

The idea here is that we first create any orbital function  $f(t) : \mathbb{R} \rightarrow \mathbb{R}^3$  and calculate numerically its derivatives at small steps  $\Delta t$ . Then we can scale it and centre it so that it fits in an image volume of size that we desire. We expect that many segments of the discrete function  $f$  will fall into every voxel in the volume and that more curved parts of  $f$  will have higher representation in the voxel than less curved parts. For every segment we can find the main direction of the orbit  $\mathbf{v} = \frac{f(t+1)-f(t)}{\Delta t}$  and calculate the rotation matrix  $\mathbf{R}$  that rotates  $\hat{\mathbf{x}} = (1, 0, 0)$  to  $\mathbf{v}$ . Then the signal for each element of the fibre for a given b-value  $b$  and a given gradient sampling direction  $\hat{\mathbf{g}}$ , is given by the following Single Tensor formula

$$\Delta S = S_0 \exp(-b\hat{\mathbf{g}}^T \mathbf{R} \Lambda \mathbf{R}^T \hat{\mathbf{g}}) \quad (24)$$

where  $S_0$  is the unattenuated signal of the fibre, and the diffusion tensor is given by

$$\Lambda = \begin{pmatrix} \lambda_{||} & 0 & 0 \\ 0 & \lambda_{\perp} & 0 \\ 0 & 0 & \lambda_{\perp} \end{pmatrix} \quad (25)$$

Therefore the total signal of the voxel for one gradient direction is given by the summations of all the contributions of the  $K$  elements in the voxel

$$S_{vox} = \sum_{i=1}^K \Delta S_i \quad (26)$$

In addition, we can generate simulations of more than one fibres by generating a single volume for every orbit and then add them all together to create complex configurations in the final volume. This is acceptable because the diffusion signal is additive i.e. the signal of a crossing of two fibres is equal to the sum of the the signals of the individual fibres. In that way we can simulate phantoms with Multi Tensor based diffusion signals as that described in eq.23. We can increase the thickness of the fibres using a typical smoothing kernel or duplicate the fibres radially. At the end we can add different levels of noise e.g. Rician or Gaussian noise with a prespecified SNR.

The method we use to create these digital phantoms offers the opportunity to simulate partial volume effects. If partial volume effects are not desired then we need to normalize with the number of fibre elements for each voxel (This function is implemented in `dipy.sims.phantom.orbital_phantom`). In fig. 1.12 we can see the volume renderings of two different phantoms created with the method described here.

### 1.8.3 Results with digital phantoms

With the purpose of comparing and visualizing the differences between the reconstruction methods described in this document we created a digital phantom of two crossing bundles. The bundles are crossing at an angle of  $90^\circ$ . The digital phantom was generated using the method described in the previous section. Here we describe the basic steps: (a) We first represented the first bundle as a discrete straight orbit starting from point  $(-1, -1, 0)$  and ending at point  $(1, 1, 0)$  with using 1000 time steps. (b) We scaled, centred and radially expanded this orbit so that it fits a volume of size  $64 \times 64 \times 64$ . This volume corresponds to the diffusion volume without any weighting. (c) We then applied the weightings for all the following volumes corresponding to

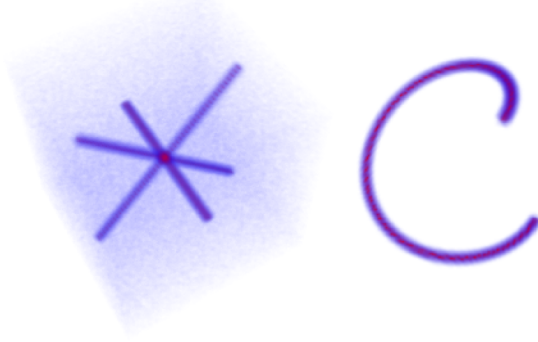


Figure 1.12: Volume renderings of the unattenuated signals of two digital phantoms. On the left 3 fibres intersect on regular angles with Rician noise of SNR=20. On the right a helicoidal fibre is shown clear of noise. For both phantoms  $S_0 = 100$  and prolate tensors with eigenvalues  $\lambda_{\parallel} = 1.4 \cdot 10^{-3} m^2/sec$  and  $\lambda_{\perp} = .35 \cdot 10^{-3} m^2/sec$  were used.

non-zero b-values. (d) We replicated the same procedure for the other bundle which initially started as an orbit from position  $(-1, 1, 0)$  and ended at position  $(1, -1, 0)$ . (e) We added the two volumes together to create an 'x' shape (see fig.1.13,1.15). (f) We added Rician noise with SNR=5. As in this document we concentrate on Cartesian Lattice Q-space acquisitions we generated b-vectors and b-values by using a keyhole Cartesian sampling grid [44] with 515 q-vectors. The maximum b-value was 11538 and the minimum was 0. Two sets of simulation experiments were performed each using a different type of Tensor.

In the first experiment shown in fig. 1.13,1.14 we used a more anisotropic prolate tensor for the simulation with eigenvalues  $\lambda_{\parallel} = 1.4 \cdot 10^{-3} m^2/sec$  and  $\lambda_{\perp} = .1 \cdot 10^{-3} m^2/sec$ . In the second experiment shown in fig. 1.15,1.16 we used a much less anisotropic prolate tensor with  $\lambda_{\parallel} = 1.7 \cdot 10^{-3} m^2/sec$  and  $\lambda_{\perp} = .3 \cdot 10^{-3} m^2/sec$ . It is well known that noise affects more less anisotropic areas. We can see this effect by comparing the overlapped FAs of these two figures (1.13, 1.15). However we can also see that all six methods (DSI, GQI, GQI2, EITL, EITL2, EITS) can resolve correctly the fiber directions by looking at their spherical distribution functions colourmaped with a standard 'jet' colourmap. For visualization purposes all ODFs are shown in relative size as they have been scaled so that their maximum values correspond to 1.

Furthermore, we can easily see that GQI is mostly similar with EITS, GQI2 is very similar with EITL and DSI is mostly similar with EITL. That DSI ODFs are very similar with EITL ODFs is expected as the two methods create theoretically the same real ODFs. Remarkably, EITL can create these ODFs without

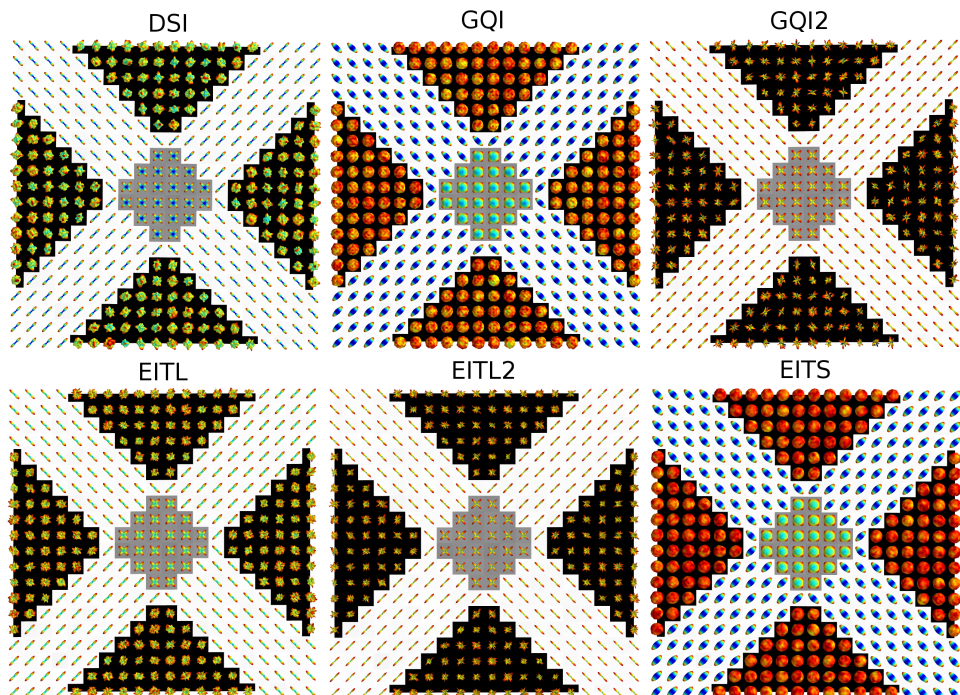


Figure 1.13: Results with an 'x' shape digital phantom. Every single tensor compartment had the following eigenvalues  $\lambda_{\parallel} = 1.4 \cdot 10^{-3} \text{ m}^2/\text{sec}$  and  $\lambda_{\perp} = .1 \cdot 10^{-3} \text{ m}^2/\text{sec}$ . Rician noise was added with SNR = 5. In this figure we can easily perceive that GQI is very similar to EITS, GQI2 is very similar to EITL and DSI is very similar to EITL. In fig. 1.14 the regions at the centers of the phantoms are depicted in higher resolution.

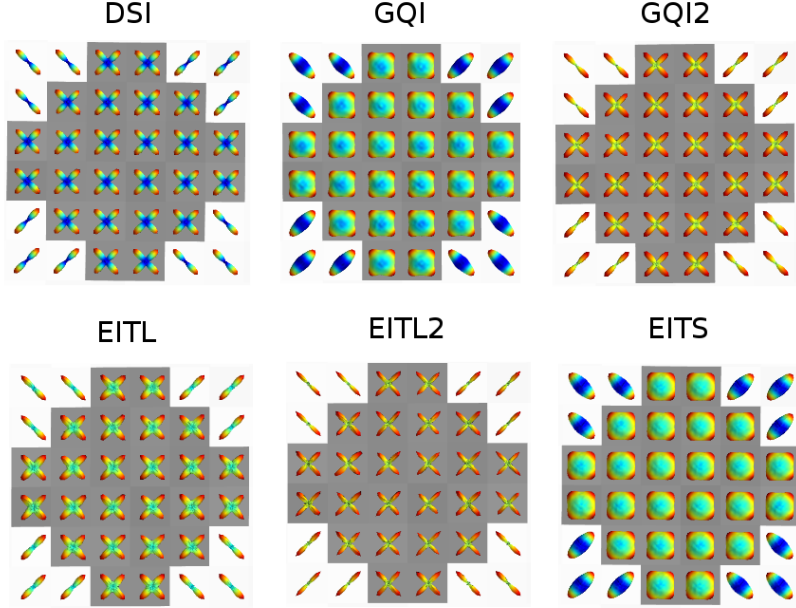


Figure 1.14: Same as previous fig. 1.13 showing the spherical distributions in the centers of the phantoms at higher resolution.

using the Fourier Transform neither using any filter or thresholds in r-space which are necessary in DSI.

Fig. 1.13, 1.15 shows that all these different grid-based reconstruction methods can reconstruct correctly the underlying fibre directions even when noise is present. However we can see that when tensors are less anisotropic the noise has a stronger effect in the resulting spherical distributions. We can also see that GQI & ETS are less sharp than DSI & EITL and these are less sharp than GQI2 & EITL2. Also DSI, GQI2, EITL, EITL2 have much lower minima than GQI and EITS.

In the EIT-based reconstruction results shown in fig. 1.14 and 1.16 we do not use any amount of smoothing as used in DSI (through hanning filter), GQI, GQI2 (through sampling length) and it is extraordinary that we obtain so well defined distributions. If we want to apply some weighting/smoothing/denoising in EIT-based methods that is simply possible through the spherical angular smoothing approach described in section 1.7.

The parameters used for these simulations were for DSI: radial sampling 2.1 – 6, hanning filter width: 36 , GQI:  $\lambda=1.2$ , GQI2:  $\lambda = 3$ , and EITS, EITL, EITL2 were all calculated with the standard options ( $z = \pm 5$ ) and no further post-processing or smoothing was used. All methods were using the same reconstruction sphere with 642 vertices and 1280 faces.

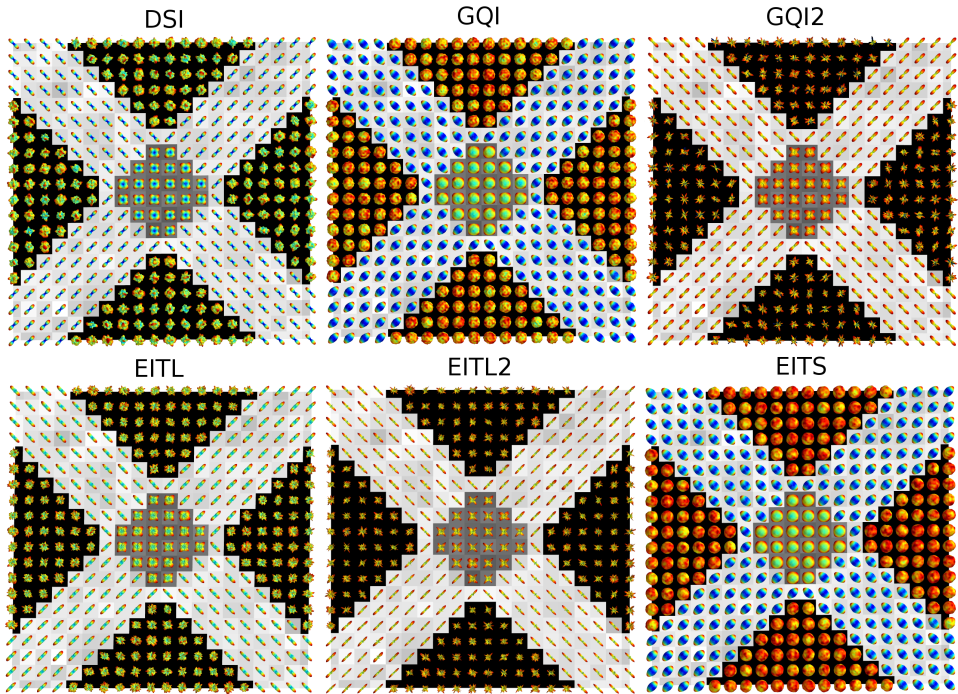


Figure 1.15: Showing the spherical distribution functions (DSI, GQI, GQI2, EITL, EITL2, EITS) of a digital phantom generated by two bundles where each bundle contains single tensors along the direction of the phantom. On the crossing area we see a dual tensor effect in every voxel. Every single tensor compartment had the following eigenvalues  $\lambda_{\parallel} = 1.7 \cdot 10^{-3} \text{ m}^2/\text{sec}$  and  $\lambda_{\perp} = .3 \cdot 10^{-3} \text{ m}^2/\text{sec}$ . Rician noise was added with SNR=5. We also visualize simultaneously the FA for this slice. We can see that in the crossing area (gray background) the FA values drop considerably however the ODFs represent precisely the crossing.

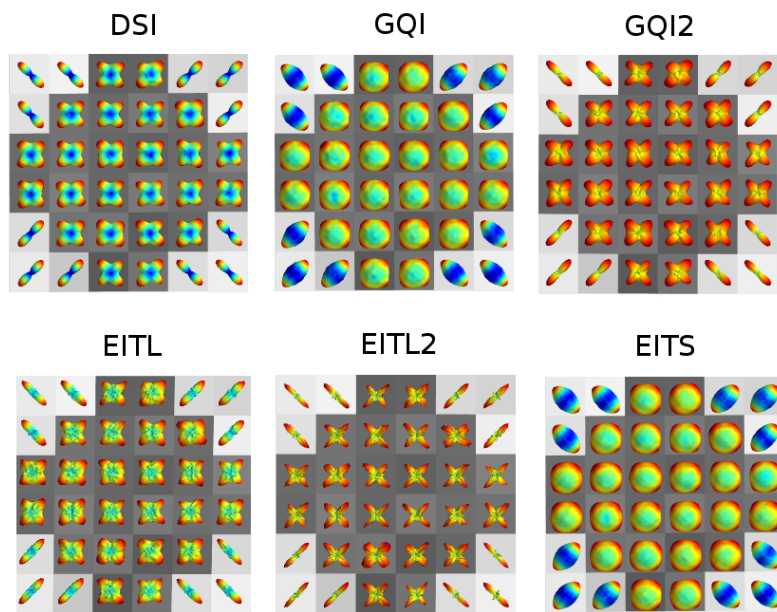


Figure 1.16: A zoomed version of previous fig. 1.15 showing the spherical distributions in the centers of the phantoms at higher resolution.

#### 1.8.4 Results with real data sets

Apparently we want to compare reconstruction methods on Cartesian grid-based acquisitions first with data sets which are rich on directions and commonly used for DSI processing. For this purpose we used a data set which was available online at cmtk.org from the Diffusion Group at Ecole Polytechnique Fédérale de Lausanne (EPFL), Switzerland. So, this data set was brought forth by a 3T scanner (TIM Trio, Siemens) with a 32 channels head coil. The field of view was  $210 \times 210 \text{ mm}^2$ , matrix size  $96 \times 96$ , and slice thickness  $3 \text{ mm}$ . 44 slices were acquired and the voxel resolution was  $2.2 \times 2.2 \times 3.0 \text{ mm}^3$ . A 258-point half grid acquisition scheme with a maximum b-value of  $8011 \text{ s/mm}^2$  also known as DSI515[48] was used. The total acquisition time was  $34 \text{ min}$  with TR= $8200 \text{ ms}$  and TE= $165 \text{ ms}$ .

The parameters used for these simulations were for DSI: radial sampling  $2.1 - 6$ , hanning filter width: 36, GQI:  $\lambda = 1.2$ , GQI2:  $\lambda = 3$ , and for EITS, EITL, EITL2 were all calculated with the standard options for zonal width ( $z = 5^\circ$ ) and spherical angular smoothing ( $s = 0.05$ ). All methods were using the same reconstruction sphere with 642 vertices and 1280 faces. The results of this experiment are shown on top of an FA slice of a healthy human in fig. 1.17 and in higher resolution in fig. 1.18. It is easily observed that EITL, EITL2 and EITS can be used for reconstructing these data sets as their results are clearly as good as the results given by DSI, GQI and GQI2. We can also easily see that EITL and EITL2 are relatively sharp which can be of an advantage for the purpose of recovering correctly the underlying real fibre directions.

We also tested our results with another human brain data set generated at a 3T scanner (TIM Trio, Siemens) in Medical Research Council Cognition and Brain Sciences Unit, Cambridge, UK. We used Siemens advanced diffusion work-in-progress sequence, and STEAM [30, 29] as the diffusion preparation method. The field of view was  $240 \times 240 \text{ mm}^2$ , matrix size  $96 \times 96$ , and slice thickness  $2.5 \text{ mm}$  (no gap). 55 slices were acquired to achieve full brain coverage, and the voxel resolution was  $2.5 \times 2.5 \times 2.5 \text{ mm}^3$ . In this experiment much less gradient vectors were used. A 102-point half grid acquisition with a maximum b-value of  $4000 \text{ s/mm}^2$  was used. The total acquisition time was only  $14 \text{ min } 21 \text{ s}$  with TR= $8200 \text{ ms}$  and TE= $69 \text{ ms}$ .

In fig. 1.19 a slice is shown where different parts of white matter are visible with the FA background image. We can clearly see structures like the CC and CST and Centrum Semiovale areas. On top of the FA the ODFs of EITL are shown. The parameters used for EITL were: a standard zonal width  $z = 5^\circ$  and spherical angular smoothing  $s = 0.05$  with the same reconstruction sphere (642 vertices, 1280 faces) as before.

For illustration purposes the upper part of fig. 1.19 is depicted again in fig. 1.20, and the region with purple shading from fig. 1.20 is given at an even higher resolution in fig. 1.21. We used Mayavi [38] a Python visualization library based on VTK to make the visualizations shown in the figures of this section.

Although much less directions were used in this acquisition scheme we

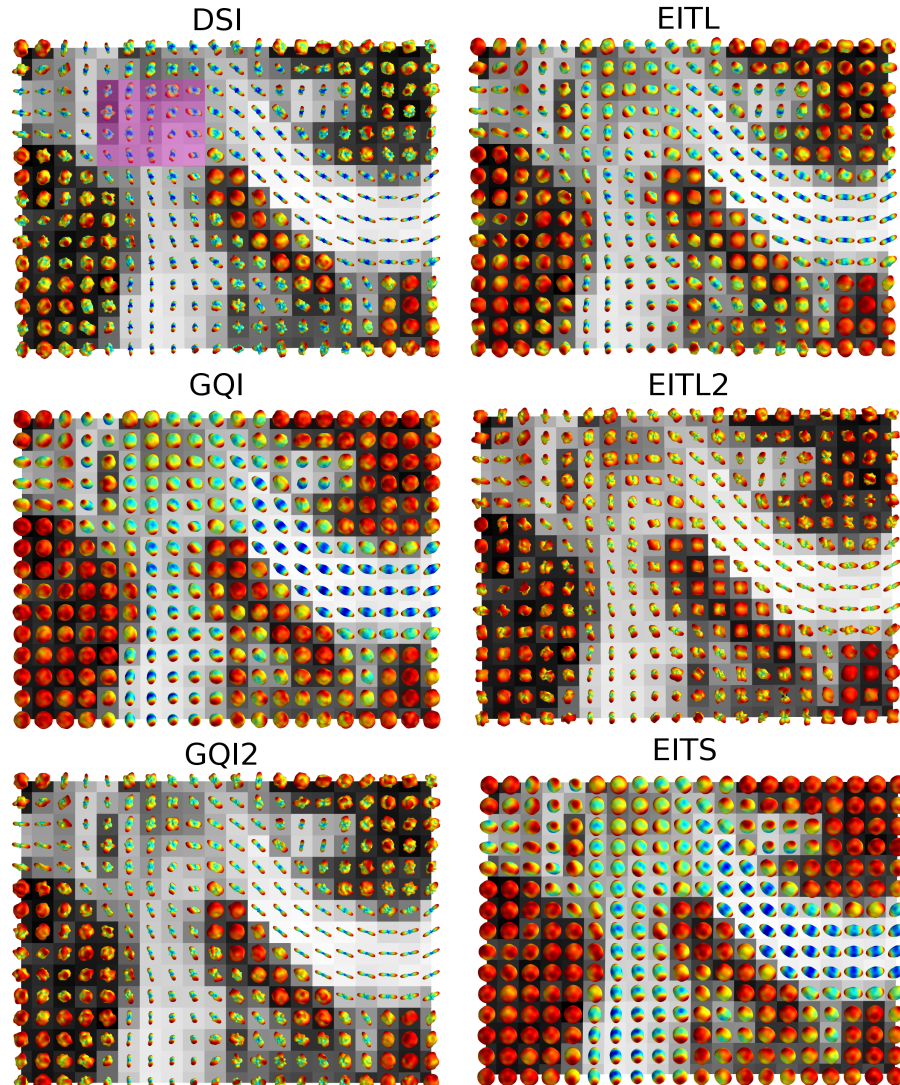


Figure 1.17: Showing the same slice of a human brain reconstructed with 6 different Cartesian grid q-space based methods. We see here that the ODFs are visualized on top of the FA slice. A clearer presentation of a region near the left upper corner (with purple shading) is given in fig.1.18 for all the 6 methods.

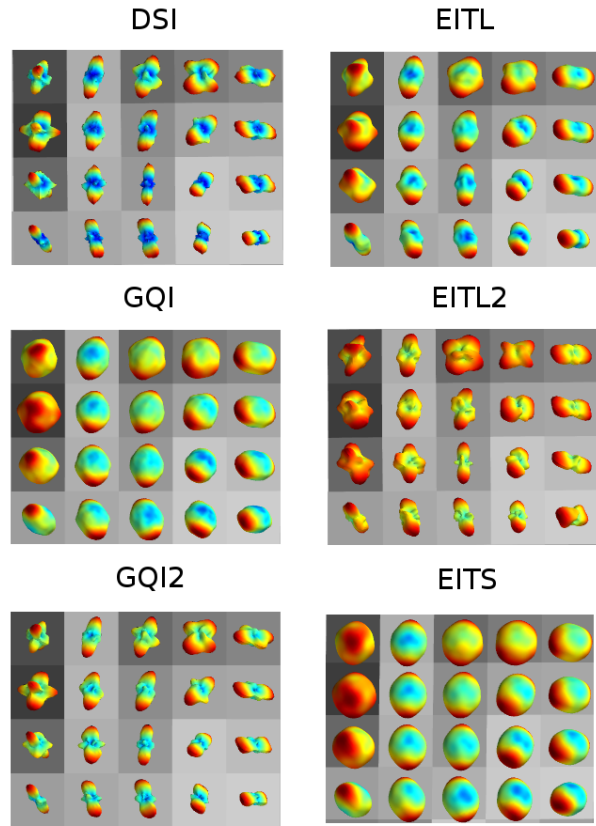


Figure 1.18: The region shown at the upper-left corner (purple shading area) in the panels of fig.1.17 is shown here at higher resolution. The data sets here are from a real human. In contrast with the results shown in simulations 1.14 we applied spherical angular smoothing with  $s = 0.05$  for EITL, EITL2 and EITS in order to remove small noisy spikes in the distributions. In addition, similarly with the results of fig.1.14 EITS is very similar with GQI but this time the difference between DSI, GQI2 and EITL, EITL2 is smaller because of the application of angular weighting.

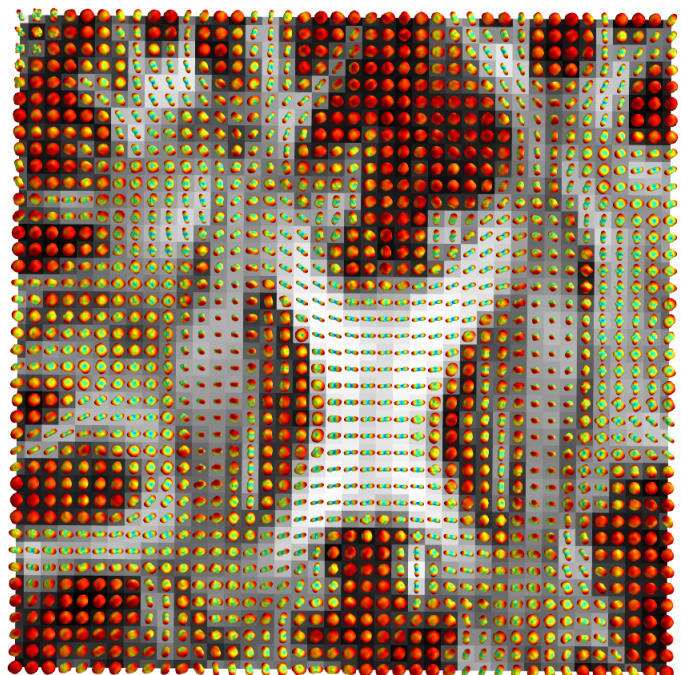


Figure 1.19: EITL ODFs rendered on top of FA of a human brain data set. A small 102-point half grid acquisition with a maximum b-value of  $4000\text{ s/mm}^2$  was used. Figures 1.20, 1.21 are zoomed versions of the same figure. We can see clearly single fibres on the CC and CST areas but also crossing fibres at the Centrum Semiovale and at the areas where big bundles cross. Also the non-white matter areas are evidently more isotropic.

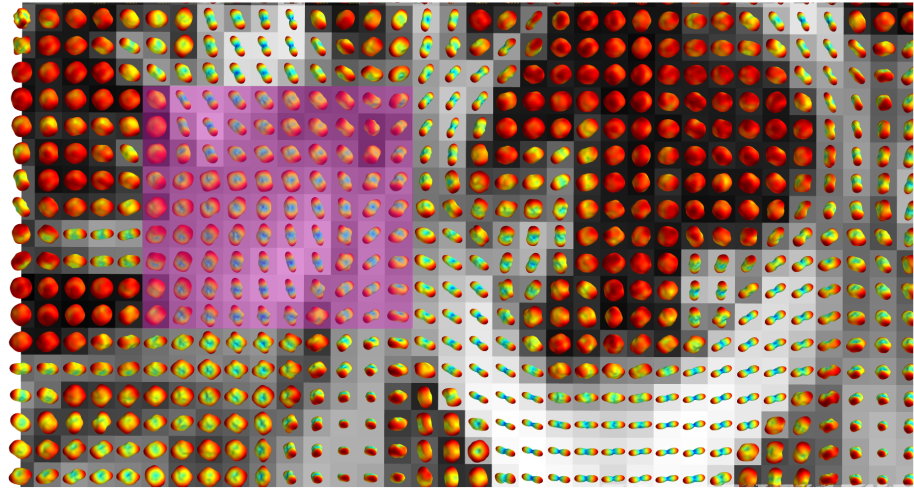


Figure 1.20: The upper part of fig. 1.19 is shown here at higher resolution. The purple shaded part is given in higher resolution in fig. 1.21

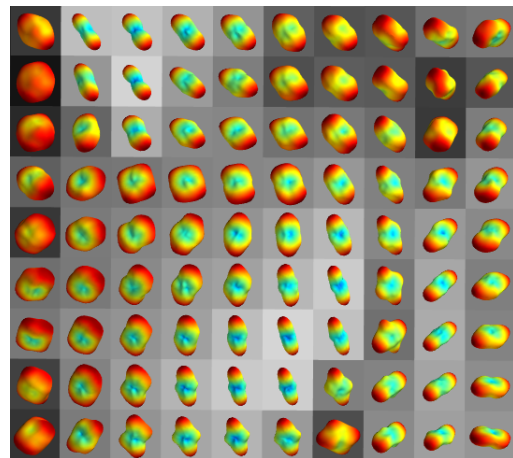


Figure 1.21: EITL ODFs of 1-fibre, 2-fibre and 3-fibre crossings from a real human data set of 101 applied weighted diffusion volume and 1 without weighting ( $b_0$ ). This picture is a zoomed version of the purple shaded area shown in fig. 1.20.

obtain a similarly accurate depiction of the underlying white matter structure in comparison with that of 258 directions. This gives great hope that we can use grid-based reconstruction methods with half-grid sequences with 100 gradient directions. This was also showed by [25] and [50] who used similar number of directions.

We can see in all the figures with real data sets single fibres as those usually found at the center of CC, and 2 or 3-fibre crossings in the intersection areas of CC with the CST and other bundles.

We can see for example in fig. 1.21 that the effect of spherical angular smoothing can help alleviate the noise effects and focus our concentration on depicting the major directions which are also of highest concern.

## 1.9 Anisotropy metrics

Until this moment we discussed about density functions on the sphere as a way to represent complex fibre directionality in the voxel. These density functions are represented as multidimensional vectors containing 200 or more dimensions in each voxel and it can be cumbersome to use them directly for subject comparisons or visualization purposes. For this purpose most people use simple scalar summarizing metrics e.g. Tensor-based FA, MD or ODF-based like the Generalized FA (GFA) [43]. In this section we will show that a similar scalar function like FA can be constructed non-parametrically. We call this NPA which stands for non-parametric anisotropy. We will also start experimenting with metrics that have more than one scalar values and can represent more accurately the directionality in each voxel that is lost with FA, GFA and MD. We will investigate and explain here the realms and robustness of Quantitative Anisotropy which was first introduced by Yeh et al. [50].

### 1.9.1 Non-parametric Anisotropy

Local voxelwise measures such as fractional anisotropy (FA), apparent diffusivity coefficient (ADC), or mean diffusivity (MD) [1,2] have been extensively adopted in clinical and applied research practice based on diffusion weighted MR imaging (dMRI). This underlines the need for valid and reliable measures which can indicate the degree of local organisation of white matter in the brain. The measures listed above are based on the parametric simple diffusion tensor (SDT) model [9] which works well when there is a single dominant fibre direction but is also known not to give valid information if the local organisation is more complex [50, 44]. We show how model-free, alternatives can yield non-parametric anisotropy (NPA). These are constructed from the GQI ODF. We apply exact analytical results which show the form of the GQI-ODF when the single tensor model is correct, and further indicate how the tensor's parameters may be estimated from this model-free approach. We compare the performance of these parametric and non-parametric measures for simulated data.

Simulations were computed for a 102-point grid sampling scheme, with a maximum b-value of  $4000\text{ s/mm}^2$ . The simulated fibre was aligned with the gradient frame of reference, and the diagonal elements of the diffusion tensor,  $D$ , were chosen to match typical values for white matter:  $\lambda_1 = 1.4 \times 10^{-3}\text{ mm}^2/\text{s}$ , and  $\lambda_2 = \lambda_3 = 0.35 \times 10^{-3}\text{ mm}^2/\text{s}$ . Variable fibre orientation was realised by spatially rotating the simulated fibres at discrete orientations. 100 orientations were used, which spanned uniformly the space of  $(\theta, \phi)$ .

In addition to the SDT a two compartment model with an isotropic component was added with volume fraction 0.5 and diffusivity  $0.7 \times 10^{-3}$ . For each acquisition scheme and fibre type, the “ideal” (noise-free) diffusion weighted signals were calculated according to the SDT model, assuming a constant ideal value of the baseline signal  $S_0 = 100$ . Complex Gaussian noise was then superimposed upon the ideal signals to provide the complex noise-contaminated signals and their magnitude was then obtained. This results in noisy values with a Rician distribution, which can be scaled in order to set the signal to noise ratio to any desired level. In this study the SNRs were 20, 40, 60, 80 and 100. The GQI ODF and SDT were fitted using dipy (dipy.org).

The GQI ODF was calculated for a tessellated spherical icosahedron with 362 vertices and 720 faces. Two values (1.2 and 3.5) were used for  $\lambda$ , the diffusion sampling length. Non-parametric FA, NPA, was calculated from the ODF by

1. locating the vertex  $V_1$  with maximum GQI ODF value  $max_1$ ;
2. with  $V_1$  as pole, locating the vertex  $V_2$  on the corresponding equatorial band of width  $\pm 5$  degrees with maximum GQI ODF value  $max_2$ ;
3. locating a vertex  $V_3$  in the equatorial band at approximately 90 degrees away from  $V_2$ , denoting the GQI ODF value of  $max_3$  at  $V_3$ .
4. With  $npd_1 = max_1^2$ ,  $npd_2 = max_2^2$ , and  $npd_3 = max_3^2$ , non-parametric anisotropy (NPA) was calculated by applying the classical FA [15] formula to the 3 values ( $npd_1, npd_2, npd_3$ ).

The rationale for the squared ODF values is based on Tuch’s formula eq.36 for ODF in the SDT case which implies that the ODF in the 3 principal axes directions of the tensor is proportional to the square root of the corresponding eigenvalue of the tensor. We have further derived an exact formula  $max_j \propto \sqrt{\lambda_j}[\Phi(cL_\Delta/\sqrt{\lambda_j}) - .5]$  where  $c$  is a constant that depends on the acquisition parameters, and  $\Phi$  is the cumulative distribution function of the standard Gaussian distribution. NEEDS PROOF?

The average NPA and FA are presented below for 200 simulations for each noise level, and single fibres with or without an isotropic component and with different diffusion sampling length. We can see that NPA gives very similar results with FA and as expected it is modulated by the degree of smoothing controlled by the value of the diffusion sampling length.

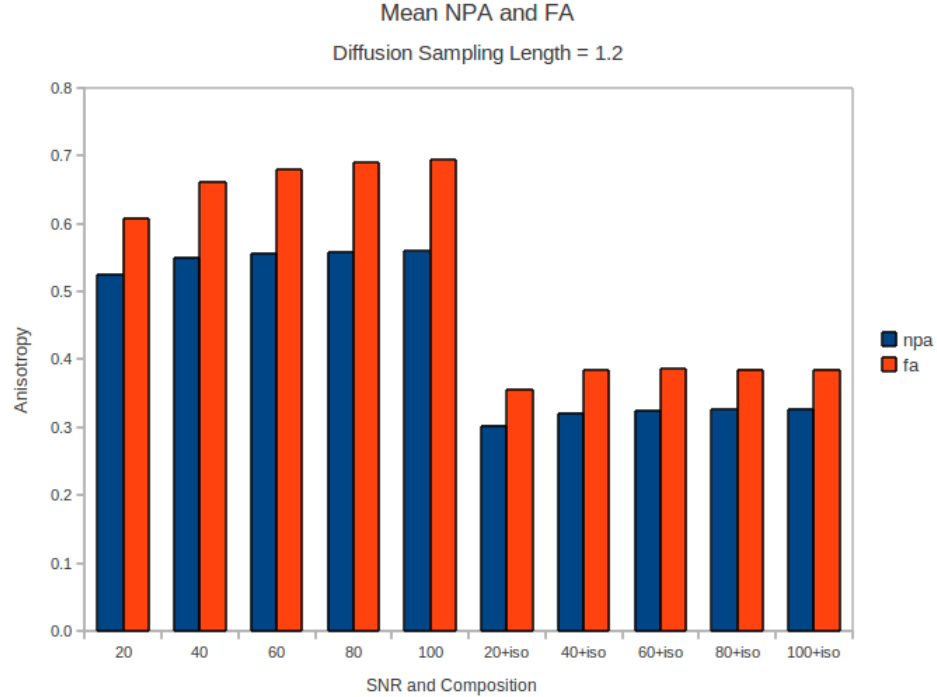


Figure 1.22: Comparison of NPA with FA for single fiber with and without an isotropic compartment at a range of signal to noise ratios.

We plan to extend this approach with voxels containing multiple peaks where FA would be unable to give an informative result and also extend it to other types of ODFs. In summary, we have shown that an informative new scalar anisotropy function (NPA) can be calculated without fitting just from the GQI ODF which promises to be a model-free proxy for FA. NPA differs from GFA [45] in that it uses just 3 values of the GQI ODF with a geometric relationship instead of the entire ODF.

### 1.9.2 Quantitative Anisotropy

Quantitative anisotropy (QA) was first used by [50] as a way to represent the peaks of the ODF with as few values as possible. This works in the following way: a) we create the ODF, b) we find the peaks using alg. 2, c) then  $QA_i$  is equal to the peak  $i$  minus the minimum value for the entire ODF. This is illustrated in fig. 1.24 where we can see a star-shaped ODF with three peaks (symmetric) ( $PK$ ). This ODF can be represented just with 3 QA values where for example the highest value will be  $QA_0 = \max(\psi_{GQI}) - \min(\psi_{GQI})$  where

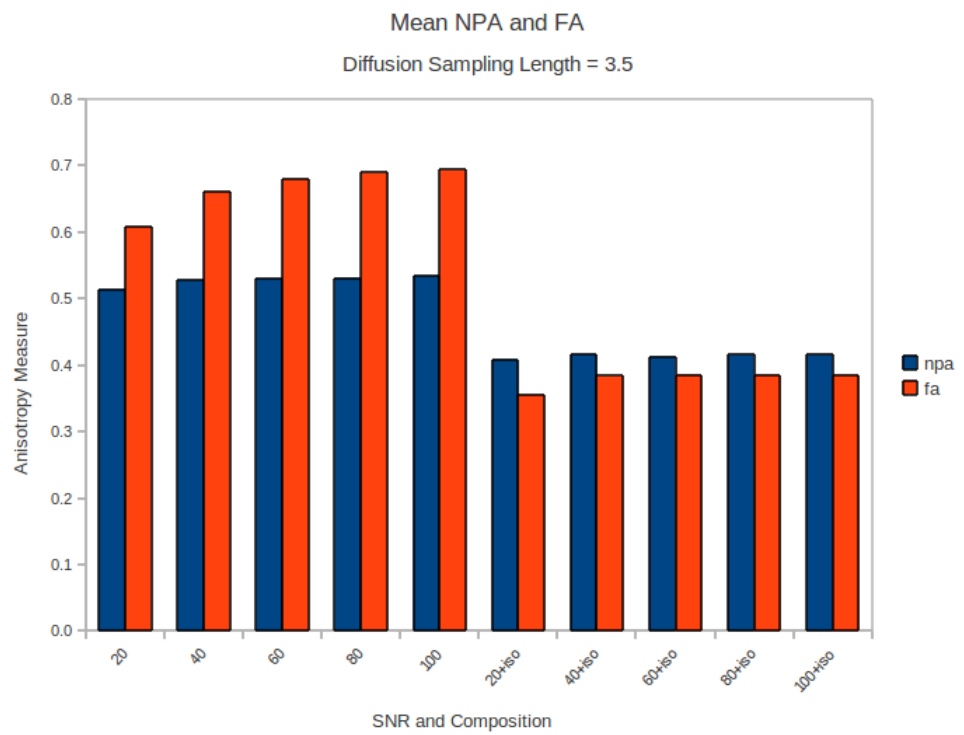


Figure 1.23: As in fig. 1.22 but with higher diffusion sampling length - less smoothing.

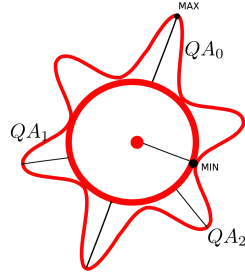


Figure 1.24: This figure shows how QA is calculated from an ODF. The sphere represents the “isotropic” component (minimum value) of a GQI ODF (star) which will be removed from the calculation of QA. QA acts like a differential component with higher values in anisotropic areas and lower in isotropic. Its big advantage over FA is that it can represent crossings.

$\max(\psi_{GQI})$  is the value of the first peak  $PK_0$ ,  $QA_1 = PK_1 - \min(\psi_{GQI})$  and  $QA_2 = PK_2 - \min(\psi_{GQI})$  with  $PK_0 \geq PK_1 \geq PK_2$ .

QA acts like a differential operator which is higher on anisotropic ODFs and lower on more isotropic. Actually for a purely isotropic ODF  $QA = 0$ . QA can be also easily normalized by the maximum ODF value of all voxels which is usually at the CSF where there is a great amount of water. If this normalization is in effect then we can very easily remove the background noise i.e. non-white matter areas, scalp, skin, muscles etc. just because these will have very low QA values. We can see this interesting property of QA in fig. 1.25. Of course the most important property of QA is that it can resolve crossings and assign a weight for every peak. We will make great use of these weightings in Chapter 3. for the creation of tractographies. Fig. 1.25 was created using DSI Studio [dsi-studio.labsolver.org](http://dsi-studio.labsolver.org) and the sequence parametrization is the same with the one provided in the experiments of the next section.

### 1.9.3 Robustness of QA

GQI was shown to have comparable accuracy to other well established q-space methods when it comes to resolving crossing fibres. In addition, this is achievable with as little as 102 points on a grid sampling scheme, bringing the total acquisition time down to a clinically acceptable level. Another advantage of GQI is that it is also applicable to a shell sampling scheme. Despite their successes in tractography applications, q-space techniques have until now failed to produce scalar metrics that could replace the ones derived from the diffusion tensor model (e.g. mean diffusivity, MD, and fractional anisotropy, FA)

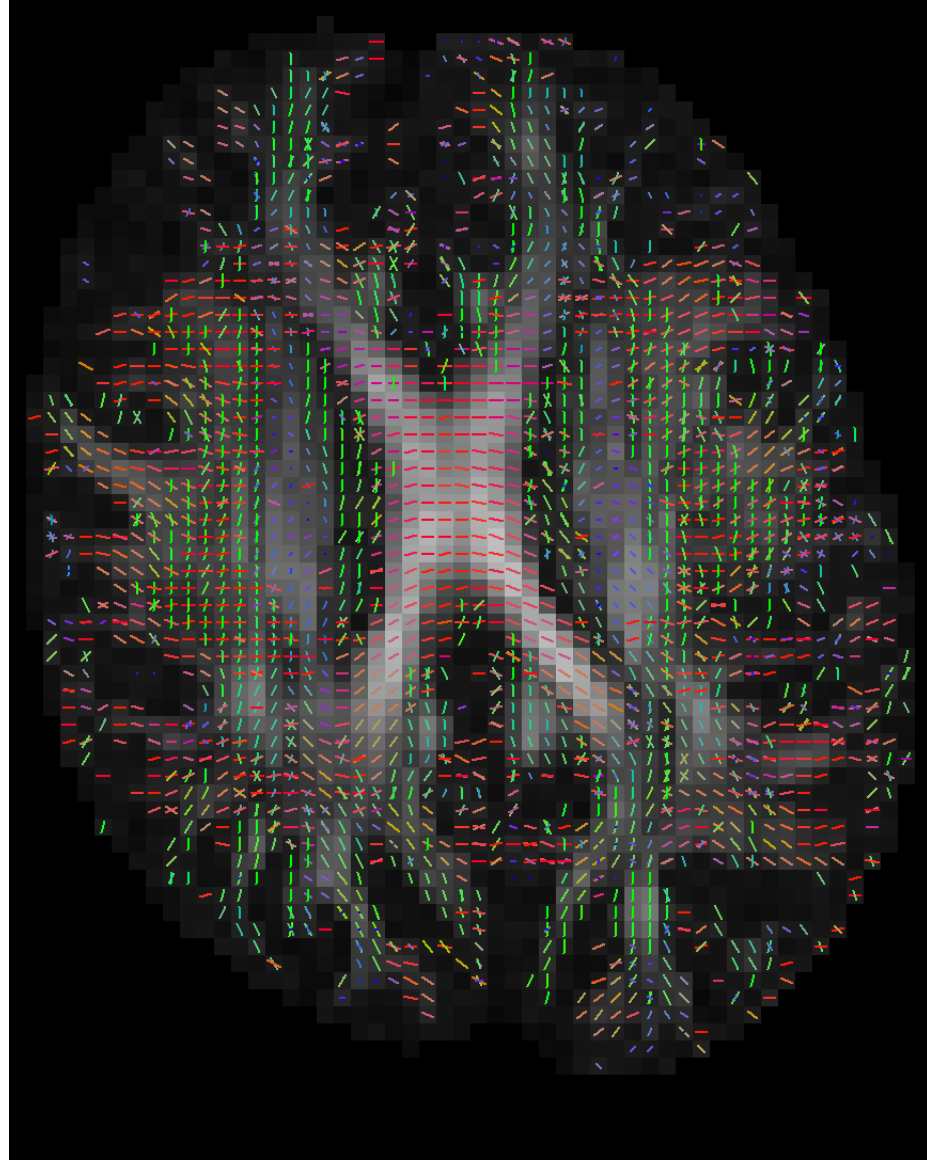


Figure 1.25: Multiple crossings of a real human data set using Quantitative Anisotropy. The first component of QA ( $QA_0$ ) is also shown in the background.

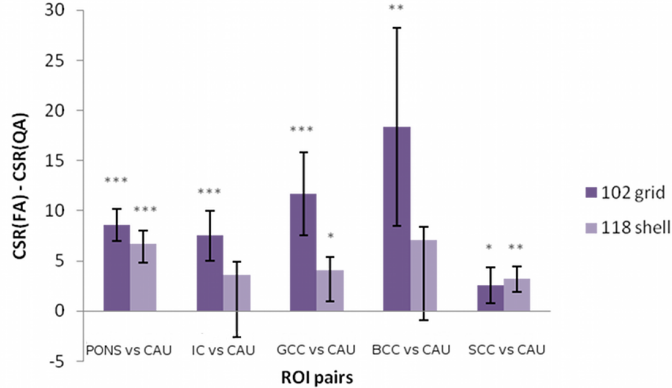


Figure 1.26: Sample results of the paired t-tests comparing CSR(FA) and CSR( $QA_0$ )

in terms of their multi-subject comparability and specificity to pathology. The data acquired with a grid sampling scheme can still be used to estimate a diffusion tensor and respective scalar parameters, but the effects of the high b-values required for q-space imaging ( $> 2000 \text{ s/mm}^2$ ) in the accuracy of the resulting DTI-based (Single Diffusion Tensor SDT) parameters has not been well characterized. The authors of GQI have also proposed a new scalar metric called quantitative anisotropy (QA) which was described in the previous sections, but its properties have not been compared to FA's. In this study we will compare the estimated values of MD, FA and  $QA_0$  (first component of QA) obtained with grid and shell sampling schemes, in terms of their precision and ability to differentiate between different brain fibre populations.

Twelve healthy volunteers aged between 18 and 40 were scanned on a 3T scanner (TIM Trio, Siemens), using Siemens advanced diffusion work-in-progress sequence, and STEAM [30, 29] as the diffusion preparation method. The field of view was  $240 \times 240 \text{ mm}^2$ , matrix size  $96 \times 96$ , and slice thickness  $2.5 \text{ mm}$  (no gap). 55 slices were acquired to achieve full brain coverage, and the voxel resolution was  $2.5 \times 2.5 \times 2.5 \text{ mm}^3$ . Two sampling schemes were considered: a 102-point grid acquisition with a maximum b-value of  $4000 \text{ s/mm}^2$ , and a single shell acquisition using 118 non-collinear gradient directions and a b-value of  $1000 \text{ s/mm}^2$ . The two acquisition schemes were matched for total acquisition time (14 min 37s), voxel resolution, and bandwidth. FA, MD and  $QA_0$  maps were then generated for each acquisition scheme and for the 12 volunteers using dipy [22](dipy.org). All the FA datasets were non-linearly registered into MNI space using FSL tools, and the same transformation parameters were applied to MD and  $QA_0$  maps. Fourteen ROIs of different brain regions were drawn in MNI space: putamen (left and right), caudate (left and right), thalamus (left and right), parasagittal white matter (left and right), pons, in-

ternal capsule (left and right), and genu, body and splenium of the corpus callosum. Small cubic ROIs were also constructed by finding the centroid of each anatomical ROI and using it as the centre for a  $3 \times 3 \times 3$  ROI. For each ROI we calculated the mean value for each metric, and the spatial coefficient of variation (CV) within the ROI (see eq. 27).

$$CV_{ROI} = \frac{\sigma_x}{\langle x \rangle} = \frac{N_{voxels} \sqrt{\sum_{x_i \in ROI} (x_i - \langle x \rangle)^2}}{\sqrt{N_{voxels} - 1} \sum_{x_i \in ROI} x_i} \quad (27)$$

The coefficient of variation of each ROI mean across subjects was also calculated, as a measure of each metric's comparability between subjects. The contrast-to-scatter ratio (CSR) (calculated for FA in eq. 28) is a good measure of a metric's ability to differentiate between different brain fibre populations [17].

$$CSR(FA) = \frac{mean(FA)_{ROI_1} - mean(FA)_{ROI_2}}{\sqrt{var(FA)_{ROI_1} + var(FA)_{ROI_2}}} \quad (28)$$

Combining the left and right versions of each ROI, we have 9 ROIs of different brain populations, which can be used to define 36 pairs of ROIs, and the CSR of all metrics was calculated for each of these pairs. Paired t-tests were then conducted to compare the performance of each metric with the two acquisition schemes, and also to compare FA and  $QA_0$  directly for each acquisition scheme.

The 102 grid sampling scheme produces significantly higher mean FA and  $QA_0$  values than the ones obtained with the 118 shell scheme, while the opposite was observed for MD. The CSR results for FA and  $QA_0$  were not significantly different between the two acquisition schemes, but the 102 grid scheme produces significantly higher CSRs for MD for 26/36 ROI pairs (fig. 1.26). For MD, no significant difference was found for the CV across subjects, but for FA and  $QA_0$  the 102 scheme produced results more comparable across the different volunteers (fig. 1.27). For FA and MD the 102 scheme showed lower CV within ROIs, especially for white matter, but no difference was found for  $QA_0$ . When comparing FA and  $QA_0$  directly, our results show that FA produces higher CSRs than  $QA_0$  for 23/36 ROI pairs for the 102 grid sampling, and for 19/36 ROI pairs for the 118 scheme. FA also shows lower variation across subjects for both acquisition schemes. Finally, FA lower CVs within white matter ROIs, while  $QA_0$  shows less variability for grey matter. The results described and shown above were obtained with the cubic ROIs, but do not differ significantly when the same analysis was applied to larger anatomical ROIs.

Our results indicate that the MD and FA maps generated from a grid sampling scheme designed for GQI are still suitable for analysis, since they do not show poorer performance when compared to a single shell and low b-value acquisition. In fact, the overall results suggest that the 102 grid sampling produces slightly more robust results than the 118 shell acquisition. A previous

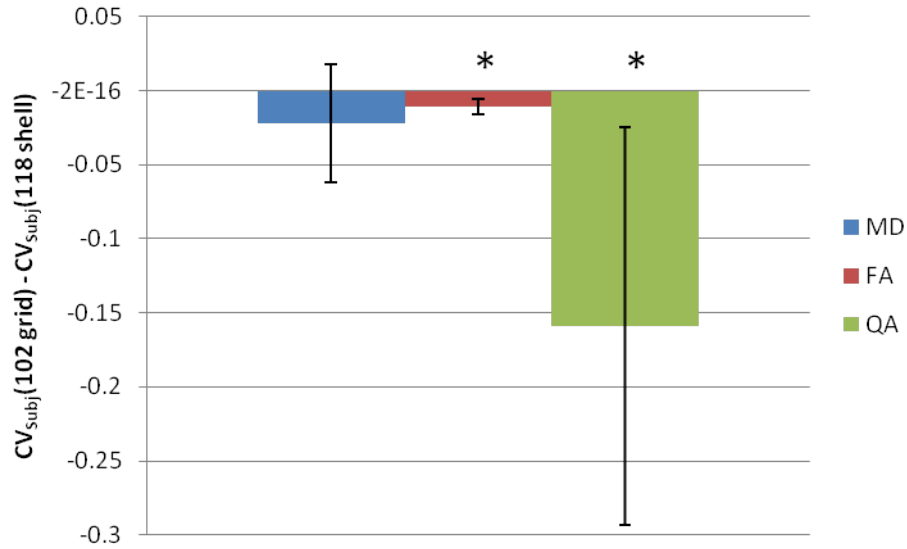


Figure 1.27: Results of the paired t-test comparing the CVs across subjects for MD, FA and QA0.

study [16] has shown that metrics such as MD and FA benefit from the use of multiple b-values, which could explain the better performance of the 102 grid scheme.

## 1.10 Discussion and Conclusion

Non-parametric methods have the advantage of representing the signal with minimum number of assumptions and without needing any fitting. For many years there has been a trend in science to prefer model-based methods rather than model free (non-parametric) perhaps because model-based can be easier to describe, easier to invent and easier to calculate Bayesian statistics with. However, there are some crucial issues with fitting: (a) Usually the interesting models have many parameters and that makes fitting very slow. (b) Commonly non-linear fitting is needed and accurate fitting is not trivial. (c) Often the model does not represent precisely the complexity of the real problem. (d) The more complex the model, the more difficult to fit [39], [26],[31].

Non-parametric methods avoid fitting and that makes them very favourable. The concentration of this document was on inventing new non-parametric methods (EIT) or comparing and extending existing ones (GQI2). We showed that a simple, fast and comprehensive transform exists that we call the Equatorial Inversion Transform (EIT). With this transform we showed that we can represent accurately the directional information of the diffusion signal. Furthermore we showed that they are many different functions ( $F$  and  $O$  see eq.

17,18,19) that can be used in order to create spherical density functions and use these to find the primary fibre directions. With a correct choose of  $F$  and  $O$  we can create theoretically the same ODF as the real ODF (DSI ODF). This can be done using EITL which is a type of EIT. Nonetheless, other density functions can be created that can identify the leading fibre directions without being real ODFs but they are still different types of spherical densities. EITL2 and EITS where examples of this last case.

Apparently, the EIT concept opens new doors for the investigation of dMRI where many new functionals can be invented in the future that stress more or less different properties of the signal. Notwithstanding, today we have already illustrated and measured that EIT has the best performance with simulations against the other stater-of-the-art methods like DSI and GQI and that empirically, EIT gives as good results with real data sets.

The EIT finds directly the ODF without creating the diffusion propagator. If for some purpose the diffusion propagator is still required then DSI or DPI [20]are favourable. It could be interesting in the future to try and recover the propagator using ideas from the EIT. However, nearly always the propagator is not needed for the analysis. Furthermore, comparing 4D densities like the propagator is a non-trivial problem, also storing the propagator for every voxel is very inefficient.

We discussed that GQI can be used for creating Quantitative Anisotropy (QA). We observed that QA acts like a differential operator but also has some similarities with FA as it is maximum on anisotropic and 0 on isotropic voxels. QA assumes that a fat isotropic part can always be removed from the ODF and that makes it more favourable for spherical functions like those of GQI and EITS. This is in contrast to sharper densities like those of DSI and GQI2 where QA is not that much useful because the minimum value of these densities will be usually near 0.

GQI needs a manually set parameter; the diffusion sampling length and in contrast the EIT is fully automatic i.e. we always just used the few default parameters for all experiments. The diffusion sampling length can be slightly different from experiment to experiment. The asset of GQI and GQI2 (which was presented together with GQI but not investigated until today) is that they are fast to compute and have simple analytical solutions. GQI2 seems robust and smooth and it has good performance both with simulations and real data.

It is important to stress that there are similarities between all these methods; DSI similar with EITL, GQI with EITS, GQI2 with EITL2. In addition we showed that we can denoise the signal using a Gaussian Spherical Angular method which operates on spherical densities and has a single parameter which is similar with the variance.

Finally, we showed that the first component of QA (highest QA value) can be used for subject comparisons in a similar way with FA. We also showed that NPA could replace FA if we want to calculate anisotropy in a completely geometric way.

The source code for all these methods can be found in dipy ([dipy.org](http://dipy.org) in module `dipy.reconst`).

## 1.11 Appendix

### 1.11.1 The cosine transform

$\int_0^\infty \cos(st)g(t)dt$  where  $g(t)$  defined on  $[t, \infty)$

Let  $f(t)$  be an even function  $f(t) = f(-t)$  defined for  $-\infty < t < \infty$

$$\begin{aligned}
F(s) &= \int_{-\infty}^{\infty} f(t)e^{its}dt \\
&= \int_0^{\infty} f(t)e^{its}dt + \int_{-\infty}^0 f(t)e^{its}dt \\
&= \int_0^{\infty} f(t)e^{its}dt - \int_{-\infty}^0 f(-t)e^{-its}dt \\
&= \int_0^{\infty} f(t)e^{its}dt + \int_0^{\infty} f(t)e^{-its}dt \\
&= \int_0^{\infty} f(t)[e^{its} + e^{-its}]dt \\
&= \int_0^{\infty} f(t)[\cos(its) + i\sin(its) + \cos(its) - i\sin(its)]dt \\
&= 2 \int_0^{\infty} f(t)\cos(st)dt
\end{aligned}$$

In the third row above we replace  $t \rightarrow -t$

If you want to compute the integral in the whole space because of symmetry you have  $F(s) = \int_{-\infty}^{\infty} f(t)\cos(st)dt$

### 1.11.2 Fourier transform of $P(\mathbf{r})r^2$

From Fourier analysis we know that if  $E(\mathbf{q})$  is the Fourier transform function of  $P(\mathbf{r})$  then

$$\begin{aligned}
\mathfrak{F}(xP(\mathbf{r})) &= i \frac{\partial E(\mathbf{q})}{\partial \mathbf{q}_x} \\
\mathfrak{F}(x^2 P(\mathbf{r})) &= - \frac{\partial^2 E(\mathbf{q})}{\partial \mathbf{q}_x^2}
\end{aligned}$$

where  $\mathfrak{F}()$  is the Fourier transform. By writing the second equation for  $y$  and  $z$  and summing them all together we obtain

$$\mathfrak{F}(r^2 P(\mathbf{r})) = - \frac{\partial^2 E(\mathbf{q})}{\partial \mathbf{q}_x^2} - \frac{\partial^2 E(\mathbf{q})}{\partial \mathbf{q}_y^2} - \frac{\partial^2 E(\mathbf{q})}{\partial \mathbf{q}_z^2} = -\nabla^2 E(\mathbf{q})$$

### 1.11.3 Radial projection of a symmetric function

Let  $f : \mathbb{R}^3 \rightarrow \mathbb{R}$  be a symmetric function with the 3D Fourier transform function  $\hat{f}(\mathbf{q})$  and  $\hat{\mathbf{u}}$  be an arbitrary unit vector. We will show that  $\int_0^\infty f(r\hat{\mathbf{u}})dr = \frac{1}{8\pi^2} \int \int_{\hat{\mathbf{u}}^\perp} \hat{f}(\mathbf{q}) q dq d\phi$  where  $\hat{\mathbf{u}}^\perp$  is the plane perpendicular to  $\hat{\mathbf{u}}$ .

Without loss of generality, we align  $\hat{\mathbf{u}}$  with the z-axis having  $\hat{\mathbf{z}} = \hat{\mathbf{u}}$ . Using the Dirac delta function (make use of Lebesgue integral) we can now write

$$\begin{aligned} \int_0^\infty f(r\hat{\mathbf{z}}) dr &= \int_0^\infty f(0, 0, z) dz \\ &= \frac{1}{2} \int \int \int_{\mathbb{R}^3} f(x, y, z) \delta(x) \delta(y) dx dy dz \end{aligned}$$

The factor  $1/2$  is required because we need the integral only in the positive half of the z-axis, and the function is symmetric. Let us define  $g(x, y, z) \equiv \delta(x)\delta(y)$ . For the two functions  $f, g : \mathbb{R}^3 \rightarrow \mathbb{R}$  with Fourier transform functions  $\hat{f}(\mathbf{q})$  and  $\hat{g}(\mathbf{q})$ , Parseval's theorem states that

$$\int \int \int_{\mathbb{R}^3} f(x, y, z) g^*(x, y, z) dx dy dz = (2\pi)^{-3} \int \int \int_{\mathbb{R}^3} f(q_x, q_y, q_z) \hat{g}^*(q_x, q_y, q_z) dq_x dq_y dq_z$$

Furthermore,  $\hat{g}(q_x, q_y, q_z) = 2\pi\delta(q_z)$  and replacing it in the above equations leads to

$$\begin{aligned} \int_0^\infty f(r\hat{\mathbf{z}}) &= \int \int \int_{\mathbb{R}^3} \frac{1}{2} f(x, y, z) g(x, y, z) dx dy dz \\ &= \frac{1}{2(2\pi)^3} \int \int \int_{\mathbb{R}^3} f(q_x, q_y, q_z) 2\pi\delta(q_z) dq_x dq_y dq_z \\ &= \frac{1}{8\pi^2} \int_{-\infty}^\infty \hat{f}(q_x, q_y, 0) dq_x dq_y \end{aligned}$$

### 1.11.4 The Tensor in GQI

We now apply this formulation under the assumption that the diffusion voxel can be represented by a single tensor model. eq. 2 can be written in the form

$$S(\mathbf{q}) = S_0 \exp(-b\mathbf{q}^T D \mathbf{q}) \quad (29)$$

where  $S_0$  is the image when b-value is equal to 0,  $b$  is the b-value for a specific direction and  $D$  is a  $3 \times 3$  matrix, known as the diffusion tensor. Then from eq. 9 and 29 the Fourier transform of  $S$  is equal to

$$Q(\mathbf{R}) = \int S_0 \exp(-b\mathbf{q}^T D \mathbf{q}) \exp(-j2\pi \mathbf{q} \cdot \mathbf{R}) d\mathbf{q} \quad (30)$$

The same equation in its triple integral form can be written as

$$\begin{aligned} Q(R) &= S_0 \iiint \exp\left(-b \sum_{i=1}^3 q_i^2 \lambda_i - j2\pi \sum_{i=1}^3 q_i R_i\right) dq_1 dq_2 dq_3 \\ &= S_0 \iiint \prod_{i=1}^3 \exp\left(-b q_i^2 \lambda_i - j2\pi q_i R_i\right) dq_1 dq_2 dq_3 \\ &= S_0 \prod_{i=1}^3 \int \exp\left(-b q_i^2 \lambda_i - j2\pi q_i R_i\right) dq_i \\ &= S_0 \prod_{i=1}^3 \int \exp\left(-b \lambda_i [q_i^2 + \frac{j2\pi R_i}{b\lambda_i} q_i]\right) dq_i \\ &= S_0 \prod_{i=1}^3 \int \exp\left\{-b \lambda_i [(q_i + \frac{j\pi R_i}{b\lambda_i})^2 + \frac{\pi^2 R_i^2}{b^2 \lambda_i^2}]\right\} \\ &= S_0 \prod_{i=1}^3 \int \exp\left\{-b \lambda_i (q_i + \frac{j\pi R_i}{b\lambda_i})^2\right\} \exp\left\{-\frac{\pi^2 R_i^2}{b\lambda_i}\right\} \end{aligned} \quad (31)$$

In that stage we could try to make use of the formula  $\int \frac{1}{\sqrt{2\pi\sigma^2}} \exp\left(-\frac{(x-\mu)^2}{2\sigma^2}\right) dx = 1$ . Now we can see that  $b\lambda_i = 1/2\sigma^2$  and  $\mu$  corresponds to  $\mu = -jR_i/b\lambda_i$ . Therefore, eq. 31 can now be written as

$$\begin{aligned} Q(\mathbf{R}) &= S_0 \prod_{i=1}^3 \sqrt{\frac{\pi}{b\lambda_i}} \exp\left(-\frac{\pi^2 R_i^2}{b\lambda_i}\right) \\ &= S_0 \left(\frac{\pi}{b}\right)^{3/2} \frac{1}{\sqrt{\prod_{i=1}^3 \lambda_i}} \exp\left(-\frac{\pi^2}{b} \mathbf{R}^T D^{-1} \mathbf{R}\right) \end{aligned} \quad (32)$$

where  $D$  is the diffusion tensor. We can replace the displacement vector  $\mathbf{R}$  with a scalar value  $L$  and a unit vector  $\hat{\mathbf{u}}$  i.e.  $\mathbf{R} = L\hat{\mathbf{u}}$  and from eq. 32 we can replace  $\frac{2\pi^2}{b} \hat{\mathbf{u}}^T D^{-1} \hat{\mathbf{u}}$  with  $k$  and  $S_0 \left(\frac{\pi}{b}\right)^{3/2} \frac{1}{\lambda_1 \lambda_2 \lambda_3}$  with  $\alpha$ . Using that last change of variables we can now write

$$\begin{aligned} \psi_Q(\mathbf{r}, \hat{\mathbf{u}}) &= \int_0^{L_\Delta} Q(\mathbf{r}, L\hat{\mathbf{u}}) dL \\ &= \alpha \int_0^{L_\Delta} \exp\left(-L^2 \frac{k}{2}\right) dL \end{aligned} \quad (33)$$

Setting  $m = \sqrt{k}L$  and using the derivation for the error function eq.33 illustrates the remarkable result that we can calculate analytically the spin ODF for Gaussian diffusion using the cumulative distribution function *CDF*.

$$\psi_Q(\hat{\mathbf{u}}) = \frac{\alpha}{\sqrt{k}} \int_0^{\sqrt{k}L_\Delta} e^{-m^2/2} dm \quad (34)$$

$$= \alpha \sqrt{\frac{2\pi}{k}} \left[ CDF(\sqrt{k}L_\Delta) - \frac{1}{2} \right] \quad (35)$$

This can be used as a check to compare the approximated/sampled spin odf that is derived in [50] with eq. 35 for the case of gaussian diffusion.

What is also very interesting is to try to derive what the normalization factor should be for the spin odf in eq.33. Because calculating a spherical integral from eq.35 seems at the moment very complicated we first work with the simpler gaussian diffusion ODF derived by Tuch [45]

$$\psi_{p_\Delta} = \frac{1}{Z} \sqrt{\frac{\pi\tau}{\mathbf{u}^T D^{-1} \mathbf{u}}} \quad (36)$$

$$\frac{Z}{\sqrt{\pi\tau}} = \iint_{S^2} (\mathbf{u}^T D^{-1} \mathbf{u})^{-\frac{1}{2}} d\mathbf{u} \quad (37)$$

Lets now define  $f_D(\mathbf{u}) = (\mathbf{u}^T D^{-1} \mathbf{u})^{-\frac{1}{2}}$ . From [32] (19.31.2) we know that we can calculate the following integral on the entire space (eq. 38). By expanding it in polar form we can find surface integral needed in eq. 37

$$MHG = \iiint f_D(x) e^{-|x|^2} dx \quad (38)$$

$$= \int_0^\infty \left[ \iint f_D(ru) du \right] e^{-r^2} r^2 dr, \quad x = ru \text{ (polar)} \quad (39)$$

However we know that  $f_D(r\mathbf{u}) = ((r\mathbf{u})^T D^{-1} (r\mathbf{u}))^{-\frac{1}{2}} = r^{-1} (\mathbf{u}^T D^{-1} \mathbf{u})^{-\frac{1}{2}}$  therefore

$$\begin{aligned} MHG &= \int_0^\infty \left[ \iint f_D(u) du \right] e^{-r^2} r dr \\ &= \iint f_D(u) du \int_0^\infty r e^{-r^2} dr \\ &= \frac{1}{2} \iint f_D(u) du \end{aligned}$$

Consequently,  $\frac{Z}{\sqrt{\pi\tau}} = 2MHG$  where MHG is the multivariate hyper-geometric function with  $\mu = -\frac{1}{2}, B = I, n = 3$  and  $\lambda_1, \lambda_2, \lambda_3$  the eigenvalues of  $\mathbf{A}$  derived from [32] (19.31.2) & (19.16.9). Therefore,

$$\begin{aligned}\frac{Z}{\sqrt{\pi\tau}} &= 2MHG \\ &= \frac{2\pi^{\frac{3}{2}}\Gamma(1)}{\sqrt{\det(I)\Gamma(\frac{3}{2})}} R_{-\frac{1}{2}}\left(\frac{1}{2}, \frac{1}{2}, \frac{1}{2}; \lambda_1, \lambda_2, \lambda_3\right)\end{aligned}$$

and  $R_{-\frac{1}{2}} = \frac{1}{2} \int_0^\infty t^0(t + \lambda_1)^{-\frac{1}{2}}(t + \lambda_2)^{-\frac{1}{2}}(t + \lambda_3)^{-\frac{1}{2}} dt$  with  $\alpha = \frac{1}{2}$  and  $\alpha' = 1$ .

Given  $\lambda_1, \lambda_2, \lambda_3$  we can integrate numerically or even possibly analytically. For the isotropic case the integral simplifies to  $\frac{1}{2} \int_0^\infty t^0(t + \lambda)^{-\frac{3}{2}} dt = \frac{1}{\sqrt{\lambda}}$  and for the cylindrical case ( $\lambda_2 = \lambda_3$ ) to  $\frac{1}{2} \int_0^\infty (t + \lambda_1)^{-\frac{1}{2}}(t + \lambda_2)^{-1} dt$ .

## References

- [1] I. Aganj, C. Lenglet, G. Sapiro, E. Yacoub, K. Ugurbil, and N. Harel. Reconstruction of the orientation distribution function in single-and multiple-shell q-ball imaging within constant solid angle. *Magnetic Resonance in Medicine*, 64(2):554–566, 2010.
- [2] Iman Aganj, Christophe Lenglet, Neda Jahanshad, Essa Yacoub, Noam Harel, Paul M Thompson, I M A Preprint Series, and Church Street S E. A HOUGH TRANSFORM GLOBAL PROBABILISTIC APPROACH A Hough Transform Global Probabilistic Approach to Multiple- Subject Diffusion MRI Tractography. pages 612–626, 2010.
- [3] DC Alexander, GJ Barker, and SR Arridge. Detection and modeling of non-gaussian apparent diffusion coefficient profiles in human brain data. *Magnetic Resonance in Medicine*, 48(2):331–340, 2002.
- [4] D.C. Alexander, P.L. Hubbard, M.G. Hall, E.A. Moore, M. Ptito, G.J.M. Parker, and T.B. Dyrby. Orientationally invariant indices of axon diameter and density from diffusion mri. *NeuroImage*, 52(4):1374–1389, 2010.
- [5] Y. Assaf and PJ. Basser. Composite hindered and restricted model of diffusion (charmed) mr imaging of the human brain. *Neuroimage*, 27(1):48–58, 2005.
- [6] Y. Assaf, T. Blumenfeld-Katzir, Y. Yovel, and PJ. Basser. AxCaliber: a method for measuring axon diameter distribution from diffusion MRI. *Magnetic Resonance in Medicine*, 59(6):1347–1354, 2008.

- [7] Y. Assaf, R.Z. Freidlin, G.K. Rohde, and P.J. Basser. New modeling and experimental framework to characterize hindered and restricted water diffusion in brain white matter. *Magnetic Resonance in Medicine*, 52(5):965–978, 2004.
- [8] A. Barmpoutis, M.S. Hwang, D. Howland, J.R. Forder, and B.C. Vemuri. Regularized positive-definite fourth order tensor field estimation from dw-mri. *NeuroImage*, 45(1):S153–S162, 2009.
- [9] PJ Basser, J Mattiello, and D LeBihan. MR diffusion tensor spectroscopy and imaging. *Biophysical journal*, 1994.
- [10] T.E.J. Behrens, H. Johansen-Berg, S. Jbabdi, M.F.S. Rushworth, and M.W. Woolrich. Probabilistic diffusion tractography with multiple fibre orientations: What can we gain? *NeuroImage*, 34(1):144–155, 2007.
- [11] Paul T. Callaghan. *Principles of Nuclear Magnetic Resonance Microscopy*. Oxford University Press, 1991.
- [12] PT Callaghan, CD Eccles, and Y. Xia. Nmr microscopy of dynamic displacements: k-space and q-space imaging. *Journal of Physics E: Scientific Instruments*, 21:820, 1988.
- [13] E.J. Canales-Rodríguez, L. Melie-García, Y. Iturria-Medina, and C.N. Cen- ter. Mathematical description of q-space in spherical coordinates: Exact q-ball imaging. *Magnetic resonance in medicine: official journal of the Society of Magnetic Resonance in Medicine/Society of Magnetic Resonance in Medicine*, 2009.
- [14] Erick Jorge Canales-Rodríguez, Lester Melie-García, and Yasser Iturria- Medina. Mathematical description of q-space in spherical coordinates: exact q-ball imaging. *Magnetic resonance in medicine : official journal of the Society of Magnetic Resonance in Medicine / Society of Magnetic Resonance in Medicine*, 61(6):1350–67, 2009.
- [15] Marta Morgado Correia. Development of Methods for the Acquisition and Analysis of Diffusion Weighted MRI Data. *Brain*, (June), 2009.
- [16] M.M. Correia, T.A. Carpenter, and G.B. Williams. Looking for the optimal dti acquisition scheme given a maximum scan time: are more *b*-values a waste of time? *Magnetic resonance imaging*, 27(2):163–175, 2009.
- [17] Williams G.B. Yeh F-C. Nimmo-Smith I. Correia, M.M. Robustness of diffusion scalar metrics when estimated with generalized q-sampling imaging acquisition schemes. In *19th Annual Meeting of the International Society of Magnetic Resonance in Medicine*, 2011.
- [18] M Descoteaux, E Angelino, S Fitzgibbons, and R Deriche. Regularized, fast, and robust analytical q-ball imaging. *Magnetic Resonance in Medicine*, vol:58no3pp497–510, 2007.

- [19] M. Descoteaux, R. Deriche, and A. Anwander. Deterministic and probabilistic q-ball tractography: from diffusion to sharp fiber distribution. 2007.
- [20] M. Descoteaux, R. Deriche, D.L. Bihan, J.F. Mangin, and C. Poupon. Multiple q-shell diffusion propagator imaging. *Medical Image Analysis*, 2010.
- [21] Maxime Descoteaux, Elaine Angelino, Shaun Fitzgibbons, and Rachid Deriche. Regularized, fast, and robust analytical q-ball imaging. *Magnetic Resonance in Medicine*, 58(3):497–510, 2007.
- [22] E. Garyfallidis, M. Brett, B. Amirbekian, C. Nguyen, FC Yeh, Y. Halchenko, and I. Nimmo-Smith. Dipy—a novel software library for diffusion mr and tractography. In *17th Annual Meeting of the Organization for Human Brain Mapping*, 2011.
- [23] Kalvis M Jansons and Daniel C Alexander. Persistent angular structure: new insights from diffusion magnetic resonance imaging data. *Inverse Problems*, 19(5):1031–1046, 2003.
- [24] J.H. Jensen, J.A. Helpern, A. Ramani, H. Lu, and K. Kaczyński. Diffusional kurtosis imaging: The quantification of non-gaussian water diffusion by means of magnetic resonance imaging. *Magnetic Resonance in Medicine*, 53(6):1432–1440, 2005.
- [25] L W Kuo, J H Chen, V J Wedeen, and W Y Tseng. Optimization of diffusion spectrum imaging and q-ball imaging on clinical MRI system. *Neuroimage*, vol:41pp7–18.
- [26] P.M. Lee. *Bayesian statistics*. Arnold London, UK:, 1997.
- [27] C. Liu, R. Bammer, B. Acar, and M.E. Moseley. Characterizing non-gaussian diffusion by using generalized diffusion tensors. *Magnetic Resonance in Medicine*, 51(5):924–937, 2004.
- [28] H. Lu, J.H. Jensen, A. Ramani, and J.A. Helpern. Three-dimensional characterization of non-gaussian water diffusion in humans using diffusion kurtosis imaging. *NMR in Biomedicine*, 19(2):236–247, 2006.
- [29] Matt A. Bernstein, Kevin F. King, and Xiaohong Joe Zhou. *Handbook of MRI Pulse Sequences*. Elsevier Academic Press, 2004.
- [30] K.D. Merboldt, W. H "anicke, H. Bruhn, M.L. Gygell, and J. Frahm. Diffusion imaging of the human brain in vivo using high-speed STEAM MRI. *Magnetic Resonance in Medicine*, 23(1):179–192, 1992.
- [31] D.C. Montgomery, E.A. Peck, G.G. Vining, and J. Vining. *Introduction to linear regression analysis*, volume 3. Wiley New York, 2001.

- [32] F.W. Olver, D.W. Lozier, R.F. Boisvert, and C.W. Clark. NIST handbook of mathematical functions. 2010.
- [33] H.H. Ong and F.W. Wehrli. Quantifying axon diameter and intra-cellular volume fraction in excised mouse spinal cord with q-space imaging. *NeuroImage*, 51(4):1360–1366, 2010.
- [34] E. Ozarslan and T.H. Mareci. Generalized diffusion tensor imaging and analytical relationships between diffusion tensor imaging and high angular resolution diffusion imaging. *Magnetic Resonance in Medicine*, 50(5):955–965, 2003.
- [35] E. Ozarslan, T.M. Shepherd, B.C. Vemuri, S.J. Blackband, and T.H. Mareci. Resolution of complex tissue microarchitecture using the diffusion orientation transform (dot). *NeuroImage*, 31(3):1086–1103, 2006.
- [36] O. Pasternak, Y. Assaf, N. Intrator, and N. Sochen. Variational multiple-tensor fitting of fiber-ambiguous diffusion-weighted magnetic resonance imaging voxels. *Magnetic resonance imaging*, 26(8):1133–1144, 2008.
- [37] V. Pickalov and P.J. Basser. 3d tomographic reconstruction of the average propagator from mri data. In *3rd IEEE International Symposium on Biomedical Imaging: Nano to Macro*, 2006, pages 710–713, 2006.
- [38] P. Ramachandran and G. Varoquaux. Mayavi: 3d visualization of scientific data. *Computing in Science & Engineering*, 13(2):40–51, 2011.
- [39] J.A. Rice. *Mathematical statistics and data analysis*. Thomson Learning, 2006.
- [40] K.E. Sakaie and M.J. Lowe. An objective method for regularization of fiber orientation distributions derived from diffusion-weighted mri. *NeuroImage*, 34(1):169–176, 2007.
- [41] J. Tournier et al. Direct estimation of the fiber orientation density function from diffusion-weighted mri data using spherical deconvolution. *NeuroImage*, 23(3):1176–1185, 2004.
- [42] J-Donald Tournier, Fernando Calamante, and Alan Connelly. Robust determination of the fibre orientation distribution in diffusion MRI: non-negativity constrained super-resolved spherical deconvolution. *NeuroImage*, 35(4):1459–72, 2007.
- [43] David S. Tuch, Timothy G. Reese, Mette R. Wiegell, Nikos Makris, John W. Belliveau, and Van J. Wedeen. High angular resolution diffusion imaging reveals intravoxel white matter fiber heterogeneity. *Magnetic Resonance in Medicine*, 48(4):577–582, 2002.
- [44] D.S. Tuch. *Diffusion {MRI} of complex tissue structure*. PhD thesis, Massachusetts Institute of Technology, Division of Health Sciences and Technology, 2002.

- [45] DS Tuch. Q-ball imaging. *change*, 2004.
- [46] V Wedeen, R Wang, J Schmahmann, T Benner, W Tseng, G Dai, D Pandya, P Hagmann, H Dâ arceuil, and A. de Crespigny, "Diffusion spectrum magnetic resonance imaging (dsi) tractography of crossing fibers,". *NeuroImage*, vol:41no4pp1267–1277.
- [47] V.J. Wedeen, P. Hagmann, W.Y.I. Tseng, T.G. Reese, and R.M. Weisskoff. Mapping complex tissue architecture with diffusion spectrum magnetic resonance imaging. *Magnetic Resonance in Medicine*, 54(6):1377–1386, 2005.
- [48] VJ Wedeen, RP Wang, JD Schmahmann, and T Benner. ... spectrum magnetic resonance imaging (DSI) tractography of crossing fibers. *Neuroimage*, 2008.
- [49] Y.C. Wu and A.L. Alexander. Hybrid diffusion imaging. *NeuroImage*, 36(3):617–629, 2007.
- [50] F Yeh, V Wedeen, and W Tseng. Generalized Q-Sampling Imaging. *IEEE transactions on medical imaging*, (c), March 2010.
- [51] F.C. Yeh, V.J. Wedeen, and W.Y.I. Tseng. Estimation of fiber orientation and spin density distribution by diffusion deconvolution. *Neuroimage*, 2011.